The Extended Mapping Obscuration to Reionization with ALMA (Ex-MORA) Survey: 5σ Source Catalog and Redshift Distribution

The Astrophysical Journal, 999:47 (20pp), 2026 March 1 https://doi.org/10.3847/1538-4357/ae2fda

The Extended Mapping Obscuration to Reionization with ALMA (Ex-MORA) Survey: 5σ Source Catalog and Redshift Distribution

Arianna S. Long[1,2], Caitlin M. Casey[2], Jed McKinney[2,40], Jorge A. Zavala[3], Hollis B. Akins[2], Olivia R. Cooper[2,41], Erini L. Lambrides[4,42], Maximilien Franco[5], Manuel Aravena[6], Matthieu Bethermin[7,8], Karina Caputi[9], Jaclyn B. Champagne[10], D. L. Clements[11], Elisabete da Cunha[12], Andreas L. Faisst[13], Fabrizio Gentile[5,14], Jacqueline Hodge[15], Allison W. S. Man[16], Sinclaire M. Manning[17,40], David B. Sanders[18], Margherita Talia[14,19], Ezequiel Treister[20], Gabriel Brammer[21], Marcella Brusa[22], Steven L. Finkelstein[2], Seiji Fujimoto[2,40], Christopher C. Hayward[23], Olivier Ilbert[8], Jean-Baptiste Jolly[24], Jeyhan S. Kartaltepe[25], Kirsten Knudsen[26], Anton M. Koekemoer[27], Daizhong Liu[28], Georgios Magdis[21,29,30], Henry Joy McCracken[31], Jason Rhodes[32], Brant E. Robertson[33], Nick Scoville[34], Kartik Sheth[35], Vernesa Smolcic[36], Justin Spilker[37], Yoshiaki Taniguchi[38], Sune Toft[21,30], C. Megan Urry[39], and Min Yun[17]

[1] Department of Astronomy, The University of Washington, Seattle, WA, USA; aslong@uw.edu
[2] Department of Astronomy, The University of Texas at Austin, Austin, TX, USA
[3] National Astronomical Observatory of Japan, 2-21-1 Osawa, Mitaka, Tokyo 181-8588, Japan
[4] NASA-Goddard Space Flight Center, Code 662, Greenbelt, MD 20771, USA
[5] CEA, Université Paris-Saclay, Université Paris Cité, CNRS, AIM, 91191, Gif-sur-Yvette, France
[6] Instituto de Estudios Astrofísicos, Facultad de Ingeniería y Ciencias, Universidad Diego Portales, Av. Ejército 441, Santiago, Chile
[7] Université de Strasbourg, CNRS, Observatoire astronomique deStrasbourg, UMR 7550, 67000 Strasbourg, France
[8] Aix Marseille Univ, CNRS, CNES, LAM, Marseille, France
[9] Kapteyn Astronomical Institute, University of Groningen, P.O. Box 800, 9700AV Groningen, The Netherlands
[10] Steward Observatory, University of Arizona, 933 N Cherry Avenue, Tucson, AZ 85721, USA
[11] Astrophysics Group, Imperial College London, Blackett Laboratory, Prince Consort Road, London SW7 2AZ, UK
[12] International Centre for Radio Astronomy Research, University of Western Australia, 35 Stirling Highway, Crawley 26WA 6009, Australia
[13] Caltech/IPAC, MS 314-6, 1200 E. California Boulevard, Pasadena, CA 91125, USA
[14] INAF—Osservatorio di Astrofisica e Scienza dello Spazio, Via Gobetti 93/3-I-40129, Bologna, Italy
[15] Leiden Observatory, Leiden University, P.O. Box 9513, 2300 RA Leiden, The Netherlands
[16] Department of Physics & Astronomy, University of British Columbia, 6224 Agricultural Road, Vancouver BC, V6T 1Z1, Canada
[17] Department of Astronomy, University of Massachusetts, Amherst, MA 01003, USA
[18] Institute for Astronomy, University of Hawai'i at Manoa, 2680 Woodlawn Drive, Honolulu, HI 96822, USA
[19] University of Bologna, Department of Physics and Astronomy (DIFA), Via Gobetti 93/2, I-40129, Bologna, Italy
[20] Instituto de Alta Investigación, Universidad de Tarapacá, Casilla 7D, Arica, Chile
[21] The Cosmic Dawn Center, Jagtvej 155A, 2200 København N, Denmark
[22] Dipartimento di Fisica e Astronomia, Università di Bologna, Via Gobetti 93/2, 40129 Bologna, Italy
[23] Center for Computational Astrophysics, Flatiron Institute, 162 Fifth Avenue, New York, NY 10010, USA
[24] Max-Planck-Institut für Extraterrestrische Physik (MPE), Giessenbachstraße 1, D-85748 Garching, Germany
[25] Laboratory for Multiwavelength Astrophysics, School of Physics and Astronomy, Rochester Institute of Technology, Rochester, NY, USA
[26] Department of Space, Earth and Environment, Chalmers University of Technology, SE-412 96 Gothenburg, Sweden
[27] Space Telescope Science Institute, 3700 San Martin Drive, Baltimore, MD 21218, USA
[28] Purple Mountain Observatory, Chinese Academy of Sciences, 10 Yuanhua Road, Nanjing 210023, People's Republic of China
[29] DTU-Space, Technical University of Denmark, Elektrovej 327, 2800, Kgs. Lyngby, Denmark
[30] Niels Bohr Institute, University of Copenhagen, Jagtvej 128, DK-2200, Copenhagen, Denmark
[31] Institut d'Astrophysique de Paris, UMR 7095, CNRS, and Sorbonne Université, 98 bis boulevard Arago, F-75014 Paris, France
[32] Jet Propulsion Laboratory, California Institute of Technology, Pasadena, CA, USA
[33] Department of Astronomy and Astrophysics, University of California, Santa Cruz, Santa Cruz, CA, USA
[34] Astronomy Department, California Institute of Technology, 1200 E. California Boulevard, Pasadena, CA, USA
[35] NASA Headquarters, 300 Hidden Figures Way, SE, Mary W. Jackson NASA HQ Building, Washington, DC 20546, USA
[36] Department of Physics, University of Zagreb, Bijenicka cesta 32, 10002 Zagreb, Croatia
[37] Department of Physics and Astronomy & George P. and Cynthia Woods Mitchell Institute for Fundamental Physics and Astronomy, Texas A&M University, College Station, TX, USA
[38] The Open University of Japan, 2-11, Wakaba, Mihama-ku, Chiba 261-8586, Japan
[39] Physics Department and Yale Center for Astronomy & Astrophysics, Yale University, P.O. Box 208120, CT 06520-8120, USA
Received 2024 August 25; revised 2025 December 11; accepted 2025 December 19; published 2026 February 23

Abstract

One of the greatest challenges in galaxy evolution over the last decade has been constraining the prevalence of heavily dust-obscured galaxies in the early Universe. At $z > 3$, these galaxies are increasingly rare, and difficult to identify, as they are interspersed among the more numerous dust-obscured galaxy population at $z = 1$–3, making

[40] NASA Hubble Fellow.
[41] NSF Graduate Fellow.
[42] NASA Postdoctoral Fellow.

efforts to secure confident spectroscopic redshifts expensive, and sometimes unsuccessful. In this work, we present the Extended Mapping Obscuration to Reionization with the Atacama Large Millimeter/submillimeter Array (ALMA; Ex-MORA) Survey—a 2 mm blank-field survey in the COSMOS-Web field, and the largest ever ALMA blank-field survey to date, covering 577 arcmin^2. Ex-MORA is an expansion of the MORA survey designed to identify primarily $z > 3$ dusty, star-forming galaxies while simultaneously filtering out the more numerous $z < 3$ population by leveraging the very negative K-correction at observed-frame 2 mm. We identify 37 significant ($>5\sigma$) sources, 33 of which are robust thermal dust emitters. We measure a median redshift of $\langle z \rangle = 3.8^{+1.7}_{-1.52}$, with two-thirds of the sample at $z > 3$, and just under half at $z > 4$, demonstrating the overall success of the 2 mm selection technique. The total integrated $z > 3$ volume density of Ex-MORA sources is $\sim$1–3 $\times$ 10^{-5} Mpc^{-3}, consistent with other surveys of infrared luminous galaxies at similar epochs. We also find that techniques using rest-frame optical emission (or lack thereof) to identify $z > 3$ heavily dust-obscured galaxies miss at least half of Ex-MORA galaxies. This supports the idea that the dusty galaxy population is heterogeneous, and that synergies across observatories spanning multiple energy regimes are critical to understanding their formation and evolution at $z > 3$.

Unified Astronomy Thesaurus concepts: Submillimeter astronomy (1647); Infrared galaxies (790); High-redshift galaxies (734); Redshift surveys (1378)

1. Introduction

Dusty, star-forming galaxies (DSFGs) are a class of extraordinarily infrared luminous ($L_{\rm IR} > 10^{12}\,L_\odot$) galaxies that are most abundant during the peak of stellar growth in the Universe ($z \sim$ 1–3; I. Smail et al. 1997; A. W. Blain et al. 2002; C. M. Casey et al. 2014). At the peak of their population prevalence, DSFGs—also known as submillimeter galaxies—are believed to be the most massive ($M_\star \sim 10^{11}\,M_\odot$) and most prolific star-forming galaxies, with star formation rates (SFRs) exceeding hundreds of solar masses per year (C. M. Casey et al. 2014; J. A. Hodge & E. da Cunha 2020). Understanding this extreme population is critical for constraining many areas of astrophysics, including extreme stellar feedback and outflow models (C. C. Hayward et al. 2021; E. Heintz & E. G. Zweibel 2022; L. Bassini et al. 2023), rapid metal enrichment of the cosmos (P. Madau & M. Dickinson 2014; X. Shen et al. 2022; J. E. Birkin et al. 2023), the formation of the first massive quiescent galaxies (S. Toft et al. 2014; F. Valentino et al. 2020; A. S. Long et al. 2023), and the collapse of dark matter halos in overdense environments at high-z (R. C. Hickox et al. 2012; C. M. Casey 2016; A. J. R. Lewis et al. 2018; A. S. Long et al. 2020; S. Lim et al. 2021). This is why, over the last two decades, it has become increasingly important to chart the prevalence, properties, and progression of DSFGs across cosmic time.

There is still mystery, however, surrounding the true abundance of luminous DSFGs in the first 2 Gyr of the cosmos, with up to 2 orders of magnitude in discrepancy across various studies at $z \gtrsim 3$ (see, e.g., A. S. Long et al. 2023; F. Valentino et al. 2023, for summaries of current estimates across the literature). This is largely because identifying $z > 3$ DSFGs is difficult: their extreme dust-obscuration makes their starlight faint, or perhaps entirely undetectable (e.g., F. Walter et al. 2012; C. C. Williams et al. 2019; S. M. Manning et al. 2022; J. McKinney et al. 2023; F. Gentile et al. 2024a), at rest-frame ultraviolet and optical wavelengths such that the typical emission lines used to secure redshifts of star-forming galaxies are attenuated beyond detection (though new JWST observations are starting to prove effective at detecting these faint lines; e.g., T. Herard-Demanche et al. 2023; M. Y. Xiao et al. 2023). Photometric redshift estimates based on the shapes of their far-IR/submillimeter spectral energy distributions (SEDs) are highly uncertain and often span a wide range of potential redshifts ($z \sim$ 1–12) due to temperature-redshift degeneracies (C. M. Casey 2020); and far-IR spectroscopic scans are expensive, as they often require integration times on the order of $\sim$1.5–3 hr *per target* due to smaller fields of view, instrument sensitivity limitations, and the need to cover a wide spectral range (e.g., F. Gentile et al. 2024b; though gravitationally lensed sources can instead take mere minutes; C. Reuter et al. 2020).

C. M. Casey et al. (2018a, 2018b) developed a backward galaxy evolution model of DSFGs based on empirical data that demonstrated how—with the appropriate depths—long-wavelength observations ($\lambda_{\rm observed} \sim$ 2–3 mm) can be an efficient way to detect DSFGs at $z > 3$, while simultaneously filtering out the more numerous $z < 3$ DSFG population. Early results leveraging this method prove promising, with several 2 mm (B. Magnelli et al. 2019; C. M. Casey et al. 2021; O. R. Cooper et al. 2022; L. L. Cowie et al. 2023) and 3 mm (J. A. Zavala et al. 2018a; C. C. Williams et al. 2019) programs identifying high fractions of $z > 3$ DSFGs in comparison to surveys at $\lambda_{\rm observed} \lesssim 1$ mm. This is the basis for the original Mapping Obscuration to Reionization with the Atacama Large Millimeter/submillimeter Array (ALMA; MORA) Survey (C. M. Casey et al. 2021; J. A. Zavala et al. 2021), a contiguous blank-field mapping survey at 2 mm in the Cosmic Evolution Survey (COSMOS) field (P. Capak et al. 2007; A. M. Koekemoer et al. 2007; N. Scoville et al. 2007). The original survey covered 184 arcmin^2 and discovered 12 robust sources, with over 70% of the sample estimated to lie at $z > 3$.

In this paper, we present an update to the original MORA Survey: the *extended* or Ex-MORA Survey. Ex-MORA is a factor of $\sim$3$\times$ larger than the original MORA survey, covering a total of 0.16 deg^2 over the COSMOS-Web Cycle 1 JWST Survey area (C. M. Casey et al. 2023). In Section 2, we present the survey design, reduction, and map characteristics. In Section 3, we present the 2 mm bright sources detected at $\geqslant 5\sigma$ in this survey, and their respective redshifts. Then, in Section 4, we present results on the cumulative number density of 2 mm sources, their redshift distributions, and highlight some interesting sample outliers, then provide our conclusions in Section 5. Where relevant, we assume a standard Λ cold dark matter cosmology with Planck-measured parameters (Planck Collaboration et al. 2020), with $H_0 = 67.4$ km s^{-1} Mpc^{-1}, and a Chabrier initial mass function (G. Chabrier 2003).

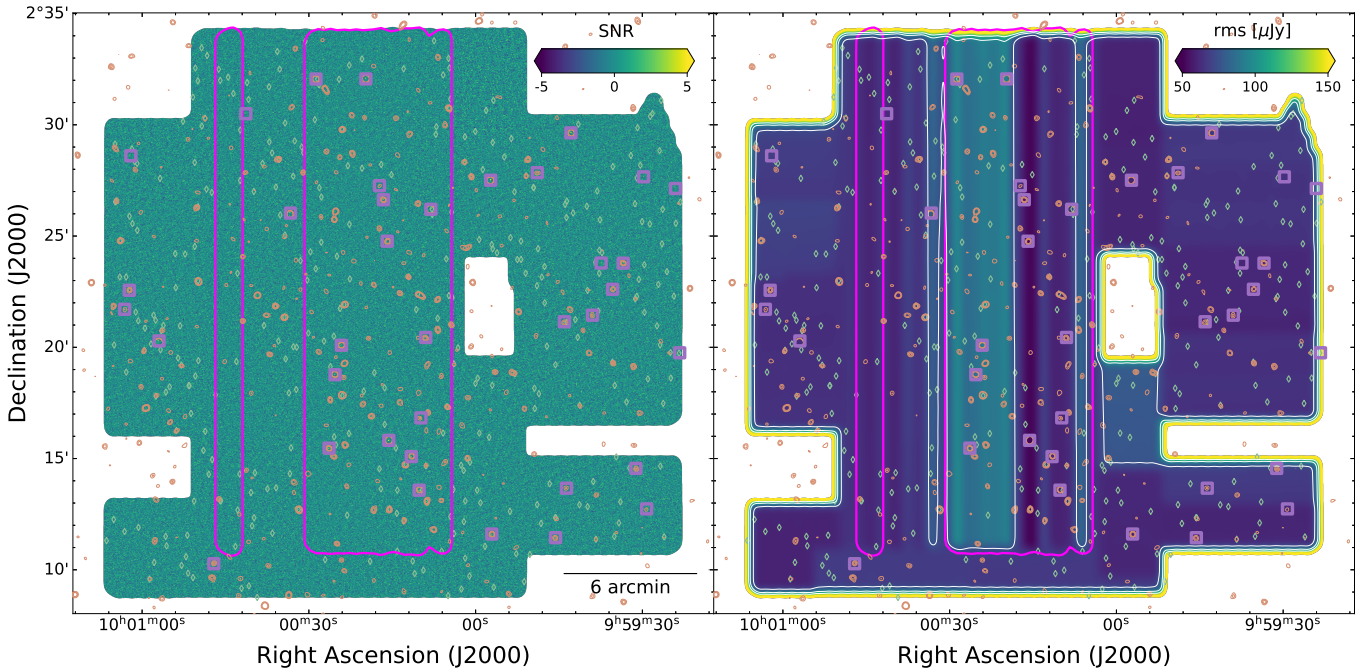

Figure 1. Signal-to-noise ratio (SNR; left panel) and rms (right panel) map of the Ex-MORA mosaic. The original MORA survey presented in Z21 and C21 is outlined in magenta. Sources at $>5\sigma$ significance are marked by purple boxes, while sources with $4\sigma <$ SNR $< 5\sigma$ are marked by green diamonds. Contours from the SCUBA-2 850 μm Survey of the COSMOS Field (J. M. Simpson et al. 2019) are overlaid in orange at levels of 3.5σ, 5σ, and 6.5σ significance. White contours on the rms map increase from 50–150 μJy beam^{-1} in steps of 25 μJy beam^{-1}.

2. The Extended Mapping Obscuration to Reionization with ALMA (Ex-MORA) Survey

The Ex-MORA Survey (ALMA Project Code 2021.1.00225.S, PI: C.M. Casey) is an extension to the MORA survey presented in J. A. Zavala et al. (2021, hereafter Z21) and C. M. Casey et al. (2021, hereafter C21). This updated survey was designed to extend the original MORA 2 mm blank-field coverage of the COSMOS-Web field (C. M. Casey et al. 2023) from 0.05 deg^2 to a contiguous 0.2 deg^2. Though A-rated, the project was only partially observed, resulting in a large, contiguous mosaic of $\sim$577 arcmin^2 or 0.16 deg^2 centered on $\alpha \approx$ 10:00:15, $\delta \approx$ +02:21:32 (shown in Figure 1). This is roughly a factor of 3 larger than the original MORA survey area (which is subsumed in the Ex-MORA map), covering roughly a third of the COSMOS-Web field. The deepest portion of the mosaic has an rms of $\sigma_{2\,\mathrm{mm}} = 51$ μJy beam^{-1}, with $\sim$90% of the map ($\sim$510 arcmin^2) at or below the proposed map depth of 90 μJy beam^{-1} (Figure 1).

Observations took place during ALMA Cycle 8, from 2022 April to 2023 January in a nominal C43-2 configuration in band 4 centered on a 147 GHz local oscillator frequency tuning. We note that the original MORA survey was proposed to be observed over two different tunings (one centered on 147 GHz and one on 139 GHz) to optimize potential detections of emission lines at $z \sim 2.5$; however, the original MORA was not completed, and most of the observed SBs were centered on 147 GHz. Thus, Ex-MORA was requested at only the one 147 GHz tuning in order to reduce overheads and to enable efficient mosaicking with original MORA survey. The 33 Ex-MORA scheduling blocks (SBs) were spatially distributed in a similar fashion as the original MORA survey. The unfinished SBs from the original MORA survey take the form of elongated "breadstick" mosaics of $\sim$149 pointings, and each of those pointings are 19.″3 offset in R.A. Newly designed Ex-MORA SBs are more square in their on-sky shape, and distributed around the perimeter of MORA, but fully aligned with the original MORA grid (following Nyquist spacing). The average phase center of each SB is reported in Table 1, along with individual noise and precipitable water vapor (PWV) properties of each SB.

The mosaic was reduced and imaged in the same manner as presented in Z21 and C21, including the following key parameters: we imaged these data using natural weighting, with a robust value =2 to optimize source signal-to-noise ratios (SNRs), set the cell/pixel size to 0.″3 (which is well below the synthesized beam size; see below), and averaged the maps over time bins of 10 s. Observations were taken under an average and favorable PWV of 1.10 mm. There are a total of 4851 individual pointings in the Ex-MORA mosaic; with 142–150 pointings per SB and an average of 22 s per pointing, this combines to a total of 29.4 hr (including overheads and calibrations). Measurement sets for the individual SBs were concatenated together using the CASA `concat` command, then reduced collectively as a mosaic. The combined mosaic has a typical synthesized beam size of $\theta_{\mathrm{FWHM}} \approx 1.''68 \times 1.''44$, which is similar to the average beam sizes across individual SBs (see Table 1). This beam size translates to physical scales of $\sim$13 $\times$ 11 kpc at $z = 3$, which is well beyond the observed physical extent of dust emission in galaxies at these epochs (J. A. Hodge et al. 2016; S. Gillman et al. 2023). Thus, it is unlikely that sources are resolved out of the map, or spatially resolved in general. Therefore, we adopt source positions and flux densities corresponding to the point of their peak signal-to-noise by identifying all of the $>5\sigma$ pixels using a "region grow" algorithm (C. M. Casey et al. 2018b; O. R. Cooper et al. 2022). Uncertainties are measured over individual source positions in the rms map shown in Figure 1 (right panel). As shown in Figure 2, the SNRs of the map pixels are well represented by a standard normal centered about zero with

Table 1
Ex-MORA Survey Observation Characteristics

SB Name	R.A.	Decl.	PWV (mm)	On-source Time (minutes)	rms (μJy beam^{-1})	Synth. Beam Size
POS-01	10:00:48.8	+02:22:30.0	0.91	37.95	87	1.″71 × 1.″43
POS-02	10:00:46.6	+02:22:30.0	1.49	37.95	89	1.″59 × 1.″44
POS-04	10:00:42.1	+02:22:30.0	1.03	37.97	91	1.″78 × 1.″47
POS-05	10:00:39.9	+02:22:30.0	1.37	37.98	85	1.″65 × 1.″40
POS-06	10:00:37.7	+02:22:30.0	1.28	37.97	94	1.″82 × 1.″35
POS-07	10:00:35.4	+02:22:30.0	1.21	37.97	91	1.″64 × 1.″43
POS-08	10:00:33.2	+02:22:30.0	1.43	38.00	112	2.″06 × 1.″28
POS-09	10:00:31.0	+02:22:30.0	1.49	38.00	93	1.″99 × 1.″28
POS-16	10:00:15.4	+02:22:30.0	0.87	37.98	78	1.″65 × 1.″40
POS-19	10:00:08.7	+02:22:30.0	1.30	38.00	83	1.″78 × 1.″37
POS-21	10:00:04.2	+02:22:30.0	1.37	37.98	89	1.″64 × 1.″52
EPOS-02	09:59:39.3	+02:31:22.3	0.97	35.28	86	1.″75 × 1.″49
EPOS-03	09:59:38.1	+02:29:12.9	1.45	39.85	88	1.″95 × 1.″39
EPOS-04	09:59:38.0	+02:27:14.8	1.47	39.82	87	1.″74 × 1.″46
EPOS-05	09:59:38.5	+02:25:20.1	1.48	37.72	90	1.″64 × 1.″51
EPOS-06	09:59:38.0	+02:23:33.0	0.65	39.83	87	1.″92 × 1.″39
EPOS-07	09:59:38.0	+02:21:37.1	0.61	39.82	84	1.″69 × 1.″48
EPOS-08	09:59:38.0	+02:19:41.2	1.47	39.83	89	1.″72 × 1.″37
EPOS-09	09:59:38.0	+02:17:45.2	0.69	39.85	90	1.″91 × 1.″30
EPOS-10	09:59:38.0	+02:15:49.3	1.01	39.85	87	1.″66 × 1.″52
EPOS-11	09:59:38.0	+02:13:53.4	1.58	39.83	94	1.″76 × 1.″48
EPOS-12	09:59:38.0	+02:11:57.5	0.66	39.83	86	1.″59 × 1.″43
EPOS-14	09:59:57.5	+02:31:35.8	0.39	39.83	79	2.″28 × 2.″03
EPOS-15	09:59:57.5	+02:26:46.0	0.56	39.87	80	1.″58 × 1.″41
EPOS-17	09:59:57.5	+02:16:56.7	1.82	39.83	105	2.″16 × 1.″29
EPOS-18	09:59:57.5	+02:12:07.0	0.84	39.82	85	1.″74 × 1.″34
EPOS-19	10:00:12.4	+02:09:55.9	1.02	38.75	94	1.″72 × 1.″36
EPOS-20	10:00:40.5	+02:10:01.6	1.76	39.82	94	1.″77 × 1.″37
EPOS-21	10:00:58.7	+02:11:09.0	0.60	38.22	84	1.″64 × 1.″51
EPOS-23	10:00:57.7	+02:18:01.7	1.65	39.85	88	1.″59 × 1.″44
EPOS-24	10:00:57.8	+02:21:27.2	1.48	39.33	111	1.″57 × 1.″42
EPOS-25	10:00:57.8	+02:24:52.8	1.55	39.85	91	1.″93 × 1.″34
EPOS-26	10:00:57.8	+02:28:18.5	0.97	39.28	89	2.″03 × 1.″45
OG MORA	⋯	⋯	⋯	⋯	60–90	1.″83 × 1.″43
Combined Mosaic	⋯	⋯	⋯	⋯	50–260	1.″68 × 1.″44

$\sigma = 1$, above which positive source peaks diverge from the distribution, demonstrating that the SNR $\geqslant 5\sigma$ threshold is an ideal threshold for low source contamination.

A series of thorough tests on survey completeness, false detection rates, and flux-boosting effects were carried out in Z21. We repeat these tests and calculate the corresponding corrections in the same fashion, and summarize briefly here. To quantify the false detection rate, we create mock noise maps that are the same size as the Ex-MORA map, with Gaussian noise distributed randomly. We then convolve this map with the average synthesized beam listed above, and re-normalize the convolved map to a standard normal distribution to represent a pure noise (source-free) map. We then count the number of serendipitous peaks at or above 5σ significance. We repeat this process 100 times, and calculate an average of $0.7^{+0.7}_{-0.5}$ of false detections in the Ex-MORA map, with an average SNR of 5.3 ± 0.2. This is in good agreement with estimates in Z21 and C21, as well as our own catalog, for which we identify one likely spurious source at the same SNR as the false detection estimates (see the next section).

Survey completeness is calculated by inserting artificial sources at random positions around the mosaic, then using the same peak finding algorithm to recover them. This process is repeated 100 times, calculating the ratio between recovered and inserted sources on each iteration. We calculate the average completeness as a function of SNR, finding ∼80% survey completeness for sources with SNRs $\geqslant 6\sigma$, while sources at 5σ–6σ are most affected with source completeness estimated at ∼50%–70%. We use these same simulations to estimate flux-boosting effects by taking the ratio of the input and recovered flux, and we find these effects to be minimal (∼5%). Finally, using these same simulations, we calculate source completeness as a function of flux density assuming various uniform rms thresholds (60, 75, and 90 μJy beam^{-1}). As shown in Figure 2, source completeness is relatively stable at ∼80% completeness for $S_{2\,\mathrm{mm}} \gtrsim 400\,\mu$Jy across each of the rms thresholds. This means that even though the map has varying noise properties, we can assume that the majority of sources with $S_{2\,\mathrm{mm}} \gtrsim 400\,\mu$Jy are well captured. Completeness drops significantly to <50% at $S_{2\,\mathrm{mm}} < 400\,\mu$Jy. These corrections are folded into the resulting on-sky number density calculation, as described in Section 4.1.

3. The 2 mm Selected Sample

In this section, we describe the Ex-MORA source catalog (listed in Table 2 and shown in Figure 3) and the ancillary data

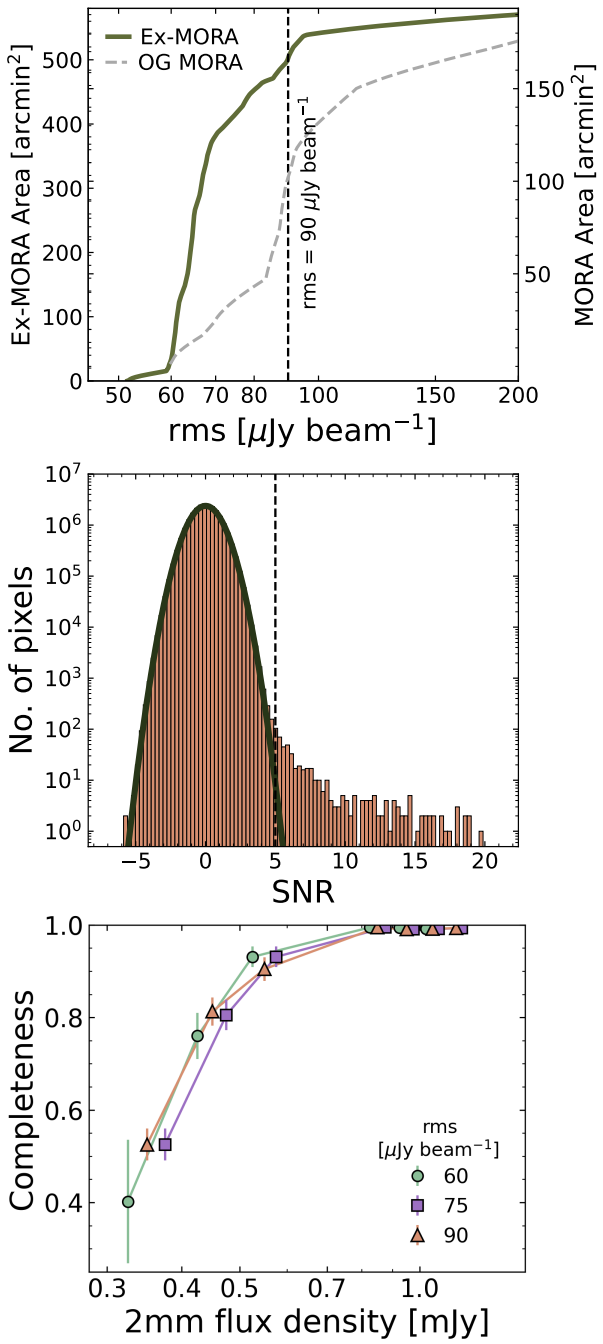

Figure 2. Top panel: cumulative distribution of the 1σ survey depth for Ex-MORA (green solid) and original (OG) MORA (gray dashed). The majority of the Ex-MORA survey (90%) has depths at or below 90 μJy beam^{-1}; this is only ∼60% for OG MORA. Middle panel: the histogram of pixel values in the signal-to-noise maps for Ex-MORA. The histogram is well fit by a standard normal (Gaussian) distribution with $\sigma = 1$ (overlaid solid line), confirming Gaussian properties of the map's noise. We see a divergence above 5σ due to the presence of positive source peaks. Bottom panel: source completeness as a function of flux given a fixed rms, calculated in flux bins of 100 μJy (points are offset for visual aid). Despite diversity in rms across the Ex-MORA map, source completeness appears stable, with 80% completeness at $S_{2\,\mathrm{mm}} \gtrsim 400$ μJy for various rms thresholds (60, 75, and 90 μJy beam^{-1}).

used to identify source counterparts and estimate their respective redshifts. The goal of this work is to update statistics on the efficiency of the 2 mm selection technique in identifying $z \gtrsim 3$ massive, dust-obscured galaxies. Detailed analysis of the physical properties, morphologies, and environments of these sources will be presented in forthcoming papers.

3.1. Ancillary Data

The Ex-MORA Survey benefits from complete coverage with the COSMOS-Web Survey (GO #1727, PIs: Casey & Kartaltepe; C. M. Casey et al. 2023), a 255 hr imaging program with contiguous coverage over 0.54 deg^2 in four JWST NIRCam filters (F115W, F150W, F277W, and F444W), and parallel MIRI imaging in the F770W band. Details on the survey design can be found in C. M. Casey et al. (2023), and details on data reduction will be described in full in M. Franco et al. (2024, in preparation). In summary, JWST NIRCam data for the epoch used in this analysis are reduced with the JWST Calibration Pipeline version 1.12.1 (H. Bushouse et al. 2023), with CRDS pmap-1170, corresponding to NIRCam instrument mapping imap-0273. We implement additional custom modifications used in other ERS and Cycle 1 surveys (e.g., M. B. Bagley et al. 2023), including subtraction of $1/f$ and background noise. NIRCam images achieve a 30 mas pixel^{-1} resolution, with astrometry aligned to the COSMOS2020 catalog (J. R. Weaver et al. 2022), which is anchored to Gaia-EDR3.

We also include a wealth of ground- and space-based optical/near-IR (OIR) data from the COSMOS2020 catalog (J. R. Weaver et al. 2022). In brief, this includes Hubble/F814W imaging (A. M. Koekemoer et al. 2007), the Spitzer Cosmic Dawn Survey (Euclid Collaboration et al. 2022), Subaru Telescope Hyper Suprime-Cam (HSC) imaging (H. Aihara et al. 2022), and UltraVISTA imaging (H. J. McCracken et al. 2012).

The COSMOS field also contains surveys across X-ray, millimeter, and radio wavelengths. Millimeter and submillimeter data includes SCUBA-2 maps at 850 μm (S2COSMOS; J. M. Simpson et al. 2019), and archival ALMA datasets collated in the A3COSMOS project (F. S. Liu et al. 2018). These data are primarily used to refine the dust SED models and accompanying photo-zs. X-ray and radio data are primarily used to discern the presence of powerful active galactic nuclei (AGN), and to quantify whether AGN emission contributes to the 2 mm flux and/or the galaxy's multiwavelength SED. For these analyses, we use data from the Chandra COSMOS-Legacy program (F. Civano et al. 2016), the Very Large Array (VLA) COSMOS 3 GHz Large Project (V. Smolčić et al. 2017), and the MeerKAT MIGHTEE-COSMOS 1.28 GHz survey (I. Heywood et al. 2022).

3.2. Optical to Mid-IR Photometry

The NIRCam counterparts to our 2 mm selected sources have resolved morphologies that can be challenging to optimally recover with standard photometric methods using circular or elliptical apertures. We tested measuring multiwavelength aperture fluxes with `SE/SE++` (E. Bertin & S. Arnouts 1996) and found the flux densities to be inconsistent between ground-based (e.g., UltraVISTA) and JWST NIRCam data above $1\sigma_{\mathrm{ground}}$. In light of these challenges, we measure fluxes using `diver` (J. McKinney et al. 2025), an empirically motivated photometry tool built to preserve the resolution of JWST when measuring point-spread function (PSF)-matched multiwavelength photometry. We now briefly summarize the methodology of `diver` below.

Table 2
Ex-MORA $\geqslant 5\sigma$ Sources

Name	Original Name	R.A. (deg)	Decl. (deg)	$SNR_{2\ mm}$	2 mm Flux Density (μJy)	z_{spec} [a]	z_{phot}
eMORA.0	MORA-0	10:00:15.62	+02:15:49.14	19.78	1023 ± 52	4.596	$4.6^{+1.2}_{-0.3}$
eMORA.1	⋯	09:59:57.28	+02:27:30.54	18.80	1133 ± 60	4.618	$1.0^{+0.1}_{-0.1}$
eMORA.2	MORA-3	10:00:08.05	+02:26:12.24	17.23	1157 ± 67	4.630	$3.4^{+0.6}_{-1.0}$
eMORA.3	⋯	09:59:42.85	+02:29:38.32	13.93	924 ± 66	4.340	$4.4^{+0.1}_{-0.1}$
eMORA.4	MORA-2	10:00:10.15	+02:13:34.74	8.78	523 ± 59	3.254[b]	$7.6^{+0.3}_{-0.5}$
eMORA.5[c]	MORA-10	10:00:16.58	+02:26:38.04	8.22	467 ± 57	2.470	$6.7^{+0.4}_{-0.4}$
eMORA.6	⋯	09:59:35.34	+02:22:36.51	8.16	501 ± 61	⋯	$3.2^{+0.3}_{-0.3}$
eMORA.7	MORA-1	10:00:19.74	+02:32:03.84	7.57	706 ± 93	3.340[b]	$3.7^{+1.0}_{-0.7}$
eMORA.8	⋯	09:59:48.89	+02:27:50.93	7.26	472 ± 65	⋯	$3.6^{+1.8}_{-1.6}$
eMORA.9	⋯	09:59:33.44	+02:23:47.0	7.23	444 ± 61	⋯	$2.5^{+0.2}_{-0.3}$
eMORA.10	⋯	10:00:56.95	+02:20:17.3	6.85	432 ± 63	2.494	$2.5^{+0.2}_{-0.2}$
eMORA.11	MORA-4	10:00:26.37	+02:15:28.14	6.64	568 ± 86	5.850	$5.4^{+1.7}_{-2.2}$
eMORA.12	MORA-6	10:00:28.71	+02:32:03.54	6.62	621 ± 94	4.76	$3.4^{+0.2}_{-0.1}$
eMORA.13	MORA-5	10:00:24.15	+02:20:05.64	6.41	579 ± 90	⋯	$5.8^{+0.5}_{-0.6}$
eMORA.14	⋯	10:00:33.32	+02:26:02.03	6.36	505 ± 79	2.510	$2.4^{+0.1}_{-0.1}$
eMORA.15[c]	⋯	09:59:37.41	+02:23:47.31	6.22	382 ± 61	0.741	$0.6^{+0.1}_{-0.1}$
eMORA.16	⋯	10:01:02.3	+02:22:33.79	6.22	397 ± 64	3.720	$3.4^{+0.1}_{-0.1}$
eMORA.17	⋯	10:01:02.04	+02:28:36.49	6.14	418 ± 68	⋯	$3.1^{+2.6}_{-0.9}$
eMORA.18	⋯	09:59:29.22	+02:12:44.3	6.12	375 ± 61	⋯	$2.5^{+0.1}_{-0.1}$
eMORA.19	⋯	09:59:38.97	+02:21:26.61	6.07	370 ± 61	⋯	$3.9^{+0.5}_{-0.5}$
eMORA.20	⋯	10:00:15.9	+02:24:46.14	6.04	318 ± 53	⋯	$4.1^{+0.1}_{-0.1}$
eMORA.21	MORA-7	10:00:11.58	+02:15:05.34	6.01	370 ± 61	⋯	$7.8^{+0.1}_{-0.1}$
eMORA.22	⋯	10:01:03.16	+02:21:42.49	5.95	378 ± 64	⋯	$7.2^{+0.5}_{-1.3}$
eMORA.23	⋯	09:59:31.16	+02:14:33.5	5.87	412 ± 70	⋯	$3.3^{+0.5}_{-0.3}$
eMORA.24	⋯	09:59:57.09	+02:11:36.53	5.81	354 ± 61	2.411[b]	$2.7^{+0.2}_{-0.2}$
eMORA.25	⋯	09:59:45.62	+02:11:26.62	5.67	345 ± 61	⋯	$2.2^{+0.1}_{-0.1}$
eMORA.26	MORA-8	10:00:25.29	+02:18:46.14	5.64	491 ± 87	2.280	$2.4^{+0.1}_{-0.1}$
eMORA.27	⋯	10:00:47.1	+02:10:16.42	5.61	379 ± 68	5.050	$3.8^{+0.8}_{-0.5}$
eMORA.28	MORA-9	10:00:17.3	+02:27:15.84	5.48	345 ± 63	⋯	$5.0^{+0.6}_{-0.5}$
eMORA.29	⋯	10:00:09.83	+02:16:49.74	5.40	325 ± 60	⋯	$3.6^{+2.6}_{-2.4}$
eMORA.30	⋯	09:59:29.78	+02:27:39.8	5.38	348 ± 65	⋯	$2.5^{+2.5}_{-0.9}$
eMORA.31[d]	⋯	09:59:23.28	+02:19:45.18	5.29	815 ± 154	⋯	⋯
eMORA.32	⋯	09:59:43.65	+02:13:40.12	5.16	345 ± 67	⋯	$2.1^{+0.1}_{-0.1}$
eMORA.33	⋯	10:00:08.97	+02:20:26.64	5.13	318 ± 62	⋯	$4.9^{+0.7}_{-3.3}$
eMORA.34	⋯	10:00:41.34	+02:30:29.93	5.06	322 ± 64	0.700	$0.6^{+0.1}_{-0.1}$
eMORA.35	⋯	09:59:44.03	+02:21:08.92	5.02	304 ± 60	⋯	$4.8^{+1.7}_{-1.1}$
eMORA.36[c]	⋯	09:59:24.03	+02:27:08.28	5.01	454 ± 91	0.710	$0.6^{+0.1}_{-0.1}$

Notes. The $\geqslant 5\sigma$ sources identified in the Ex-MORA Survey. Spectroscopic redshifts (if available) are listed in the z_{spec} column, while photo-zs (estimated via BAGPIPES or CIGALE) are listed with their 68% confidence intervals in the z_{phot} column. When available, spectroscopic redshifts are used over photometric redshifts.
[a] All spectroscopic redshifts are compiled in A. A. Khostovan et al. (2025), with the original surveys as follows. Rest-frame optical/UV redshifts are from S. J. Lilly et al. (2007), J. R. Trump et al. (2007), M. Kriek et al. (2015), P. Stott et al. (2016), T. Nanayakkara et al. (2016), Z. C. Marsan et al. (2017), G. Hasinger et al. (2018), E. Wisnioski et al. (2019), B. Vanderhoof et al. (2026, in preparation), J. Kartaltepe et al. (2026, in preparation), and P. Capak et al. (2026, in preparation). CO-derived redshifts are from M. S. Yun et al. (2015), S. Jin et al. (2019), C. M. Casey et al. (2019), E. F. Jiménez-Andrade et al. (2020), C.-C. Chen et al. (2022), and Chen et al. (2026, in preparation).
[b] The spec-zs for these sources are based off single CO line detections (with additional supporting information from their photo-z probability distributions; see Appendix A.1).
[c] These sources have significant synchrotron emission without which they would not be detected in this survey.
[d] This source is likely spurious; see Section 3.

For each of our sources, `diver` proceeds through the following: first, we make $50'' \times 50''$ cutouts around the target in the science image and error/weight image from which a flux will be measured. This includes JWST NIRCam and MIRI data (F115W, F150W, F277W, F444W, and F770W) as well as all multiwavelength imaging data compiled in the COSMOS field as of COSMOS2020 (CFHT, HSC, Hubble Space Telescope, HST, and UVISTA; Spitzer, J. R. Weaver et al. 2022). Next, we create a segmentation map using `photutils` (L. Bradley et al. 2023) from the NIRCam/F444W map, and in some cases include an additional de-blending step to isolate the source from its neighbors. We adopt the arbitrarily shaped segmentation boundary (down to an SNR-per-pixel of 3) of the source as an aperture through which to measure all

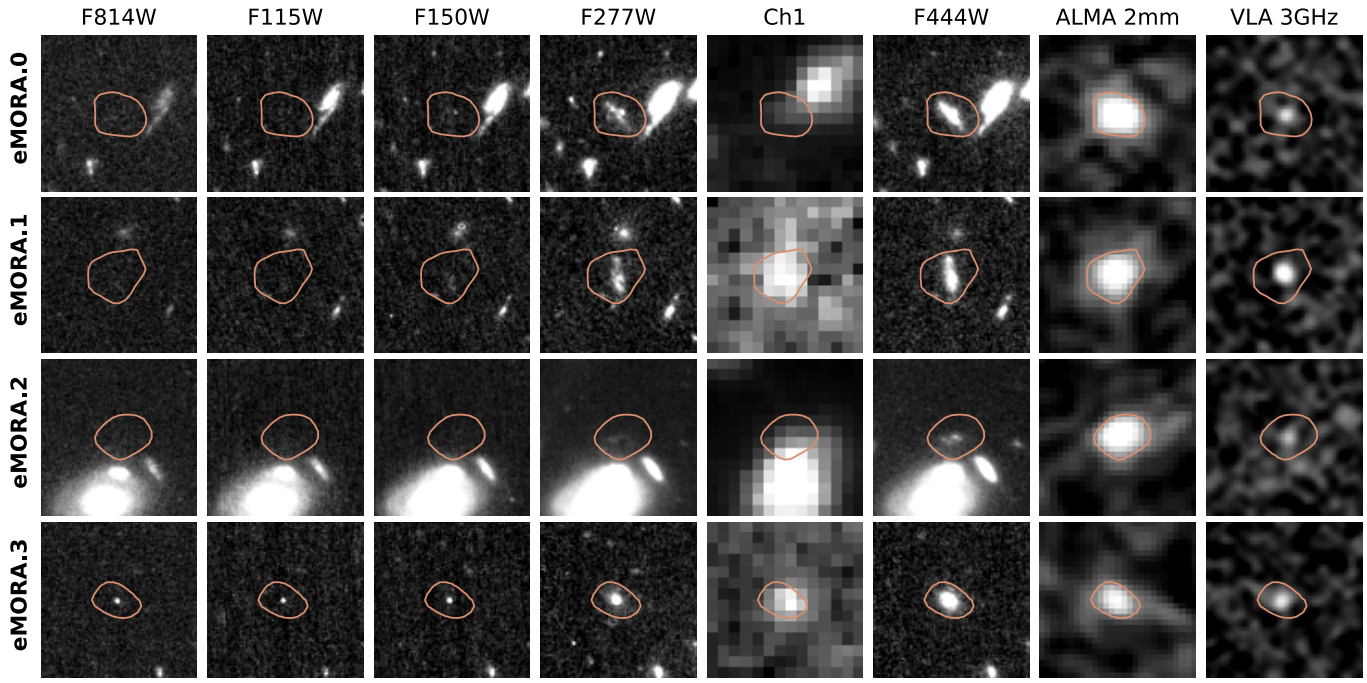

Figure 3. Multiwavelength cutouts of the 5σ Ex-MORA sample. Cutouts are $8'' \times 8''$ and all are overlaid with a 5σ contour from the 2 mm data. From left to right: Hubble Space Telescope (HST) Advanced Camera for Surveys (ACS) F814W from A. M. Koekemoer et al. (2007), N. Scoville et al. (2007); JWST/NIRCam F115W, F150W, F277W from C. M. Casey et al. (2023); Spitzer/IRAC channel 1 from M. L. N. Ashby et al. (2015); JWST/NIRCam F444W from C. M. Casey et al. (2023); ALMA 2 mm from this paper; and the Very Large Array (VLA) 3 GHz from V. Smolčić et al. (2017). All (real) sources are detected at minimum in the F444W band, and all but three are detected significantly also in the F277W band. This figure is continued in the Appendix.

multiwavelength photometry. An example of this aperture is presented in Figure 2 of J. McKinney et al. (2025). We measure the flux through this aperture in every image and, for lower-resolution data (e.g., ground-based and Spitzer IRAC data), multiply by a PSF correction factor that accounts for the flux loss due to aperture corrections. We measure flux uncertainties from the local background summed in quadrature with the shot noise, readout noise, and dark current noise all bootstrapped from the error/weight maps using the arbitrarily shaped aperture to faithfully capture the noise scaling per pixel. More details and equations describing this process are described in J. McKinney et al. (2025).

The JWST NIRCam (F115W, F150W, F277W, and F444W) fluxes and flux errors measured with `diver` are generally consistent with the aperture fluxes from `SE/SE++` within $1\sigma_{\rm diver}$, but not within $1\sigma_{\rm SE/SE++} \ll \sigma_{\rm diver}$. Most notably, the multiwavelength fluxes from `diver` are far more consistent between ground-based and JWST data given the expected shape of the rising SEDs into the near-infrared.

All but three of the Ex-MORA galaxies are significantly detected (SNR $>=$ 3) in at least three bands between the CFHT u-band ($\lambda \sim 3600$ Å) and Spitzer IRAC channel 4 ($\lambda \sim 8\,\mu$m); these three are either confirmed or predicted $z > 5$ galaxies. Of the remaining sample, more than 90%, 75%, and 66% have $n \geqslant 4$, 5, and 6 significant detections, respectively, across these wavelengths. Almost all galaxies are detected in both F277W and F444W, and most are also detected in IRAC channels 1 and 2. Given the goals of the 2 mm selection technique to identify high-z heavily dust-obscured galaxies, it is unsurprising that, in general, detection drops off significantly at $\lambda_{\rm obs} < 1.5\,\mu$m. Finally, all sources covered by MIRI F770W are detected ($n = 15$). As seen in the literature, the addition of JWST imaging marks significant improvement in capturing the rest-frame optical continuum of high-z dusty sources (S. Gillman et al. 2023; S. M. Manning et al. 2025). Indeed, looking at non-JWST data, roughly a third of the sample would have three or fewer detections, and ~60% have at least four detections.

3.3. Source Selection

As mentioned in Section 2, we adopt source positions and flux densities corresponding to the point of their peak signal-to-noise using a "region grow" algorithm for peaks at or above 5σ significance. Overall, 37 sources are identified in the combined Ex-MORA map at or above 5σ significance, with 11 of the original 13 MORA sources recovered (C21). One of the missing original sources (MORA-12) was already believed to be spurious due to lack of detection at any other wavelengths and proximity to the edge of the original maps (C21). In the combined Ex-MORA mosaic, the rms at the edges of the original MORA map—where MORA-12 was discovered—are improved. In this new mosaic, MORA-12 disappears entirely, thus confirming its nature as a false object. The other original MORA source (MORA-11) is recovered with an SNR of 4.9σ and, therefore, just misses the 5σ threshold for inclusion in this work.[43] We report source coordinates, relevant flux densities, and estimated and/or spectroscopic redshifts for the 37 sources detected at $\geqslant$5σ in Table 2, and show multiwavelength cutouts of these sources in Figure 3. Sources are numbered in inverse

[43] The extracted flux density for this source from the Ex-MORA map is well within uncertainty of the previous measurement (original $S_{2\,\rm mm} = 356 \pm 69\,\mu$Jy versus new $S_{2\,\rm mm} = 334 \pm 68\,\mu$Jy), and therefore, the discrepancy is not likely an issue with the data reduction and measurement process, but instead likely due to boosting from a coincident noise fluctuation.

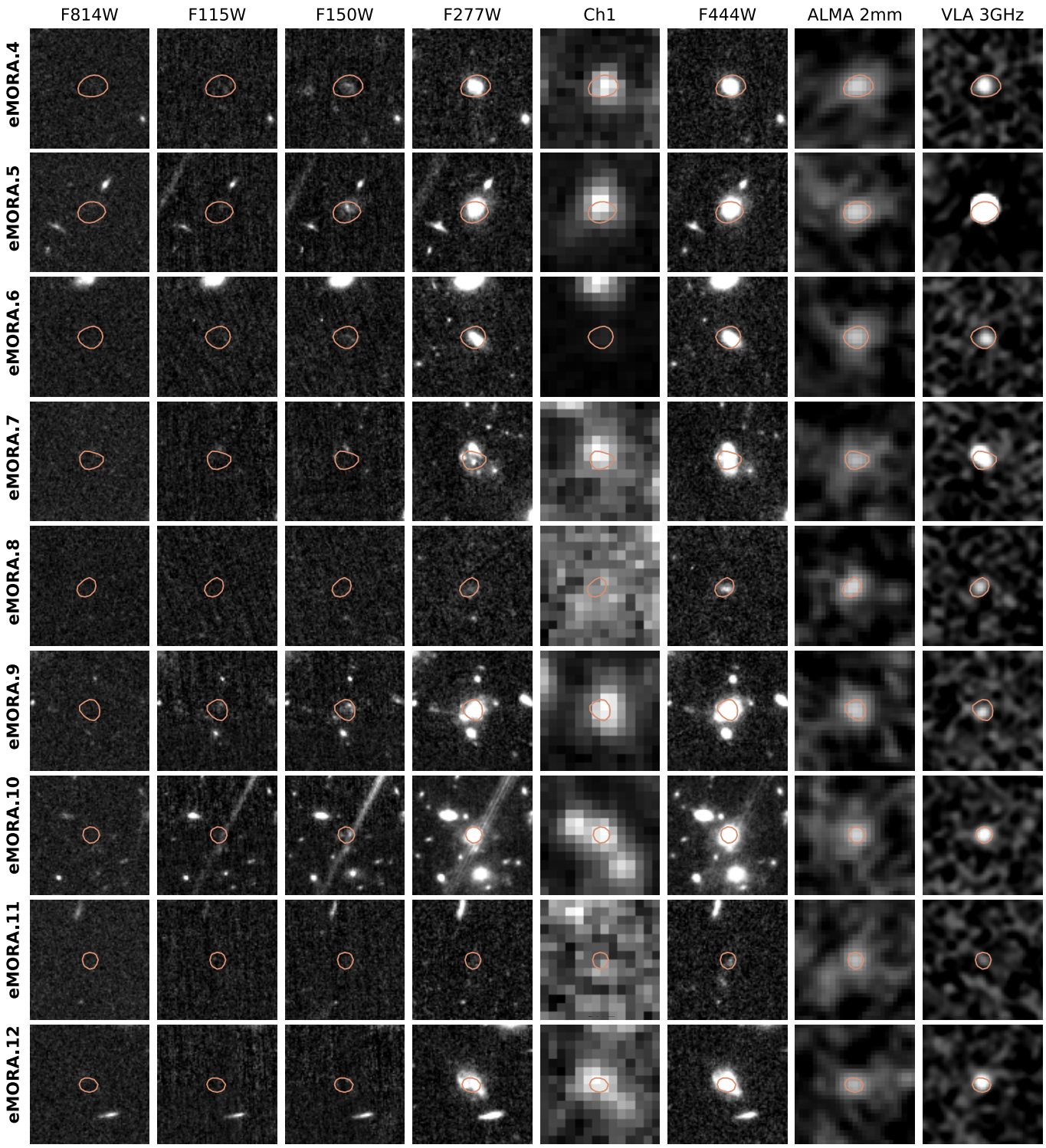

Figure 3. (Continued.)

order according to their 2 mm SNRs, with eMORA.0 having the highest SNR across the sample.

Of the 37 sources, 36 (∼97%) are detected at wavelengths $\lambda_{\rm observed} < 8\,\mu$m, and 31 (∼84%) are detected with SCUBA-2 at 850 μm. All sources are detected at minimum in the F444W band, with the exception of one source—eMORA.31. This source is also not detected in any Spitzer IRAC bands nor SCUBA-2 imaging, has no ancillary ALMA or radio detections, and is on the edge of the map in a noisy region; thus, we believe this source likely a positive noise fluctuation. We remove eMORA.31 from the analyses in this work, though keep it listed in the Table for posterity.

In C21, MORA-10 (herein eMORA.5) had reported synchotron emission significant enough to boost the 2 mm emission such that without this component, this source would not meet the detection threshold of the survey. Using data from the VLA-COSMOS and MIGHTEE-COSMOS surveys, we find that 23/36 sources have detections at both the 1.28 and

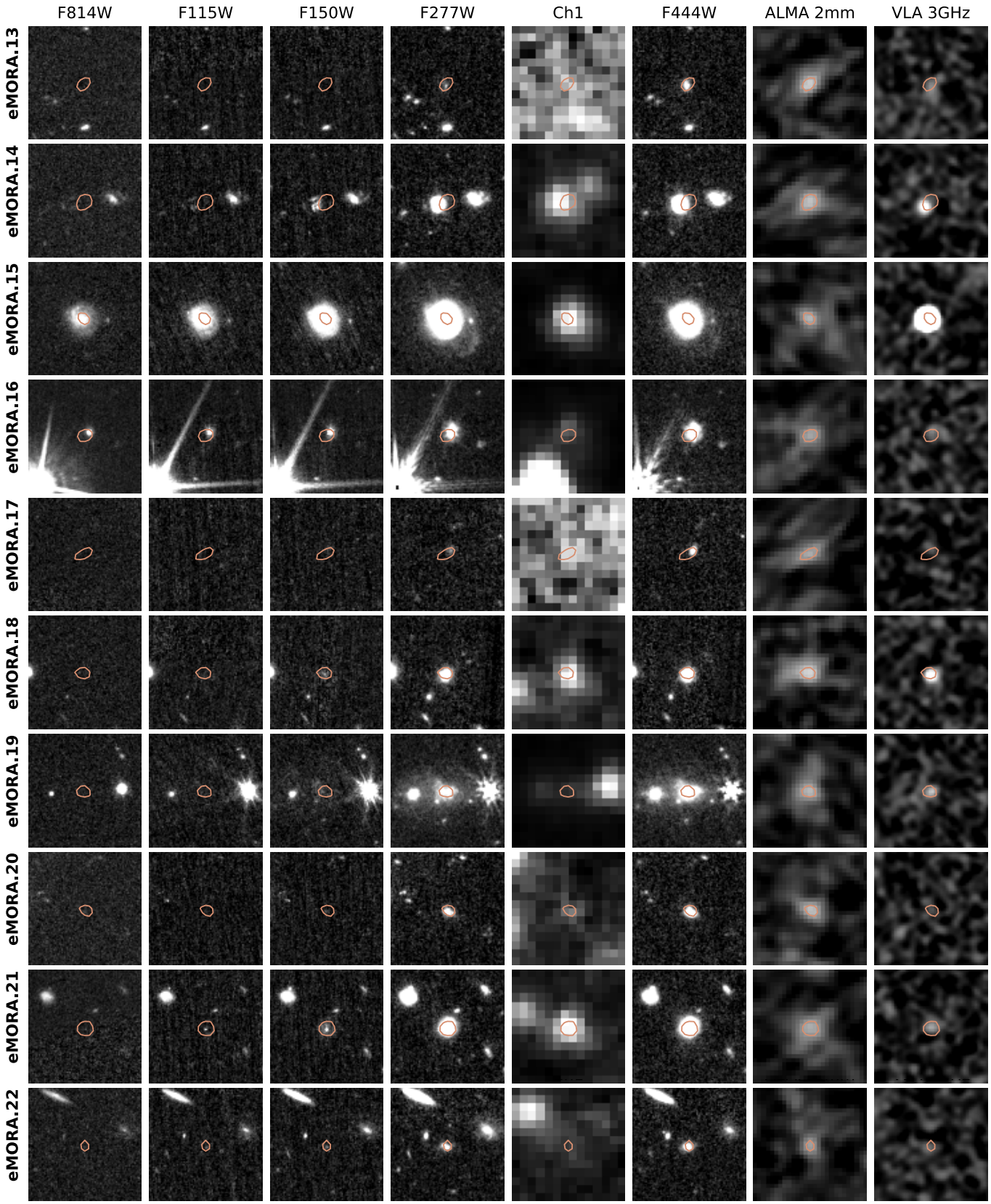

Figure 3. (Continued.)

3 GHz frequencies. Using these detections, we calculate synchrotron slopes and extend this to the 2 mm wavelength. We find that most sources ($n = 20$, or ∼87%) have estimated subpercent levels of synchrotron emission in the 2 mm band. Two out of the three remaining sources are previously identified $z \sim 0.7$ AGN (eMORA.15 and eMORA.36;

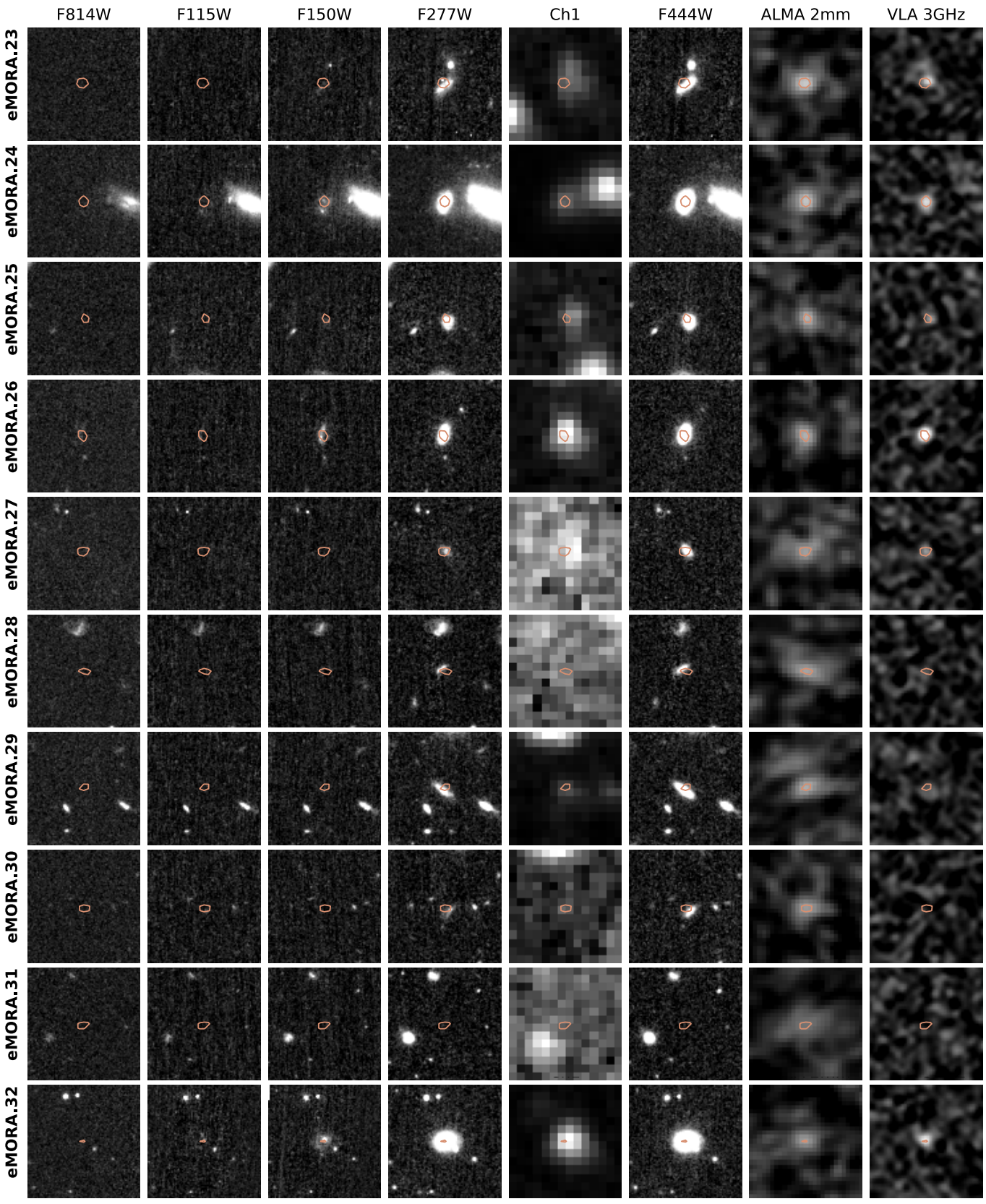

Figure 3. (Continued.)

J. R. Trump et al. 2007), while the third is the spectroscopically confirmed $z = 2.57$ MORA-10/eMORA.5 source previously discussed in C21, and spectroscopically confirmed in M. Kriek et al. (2015). None of these three sources would meet our survey thresholds without significant boosts ($\gtrsim$40% of total 2 mm flux) from their synchrotron emission. The two

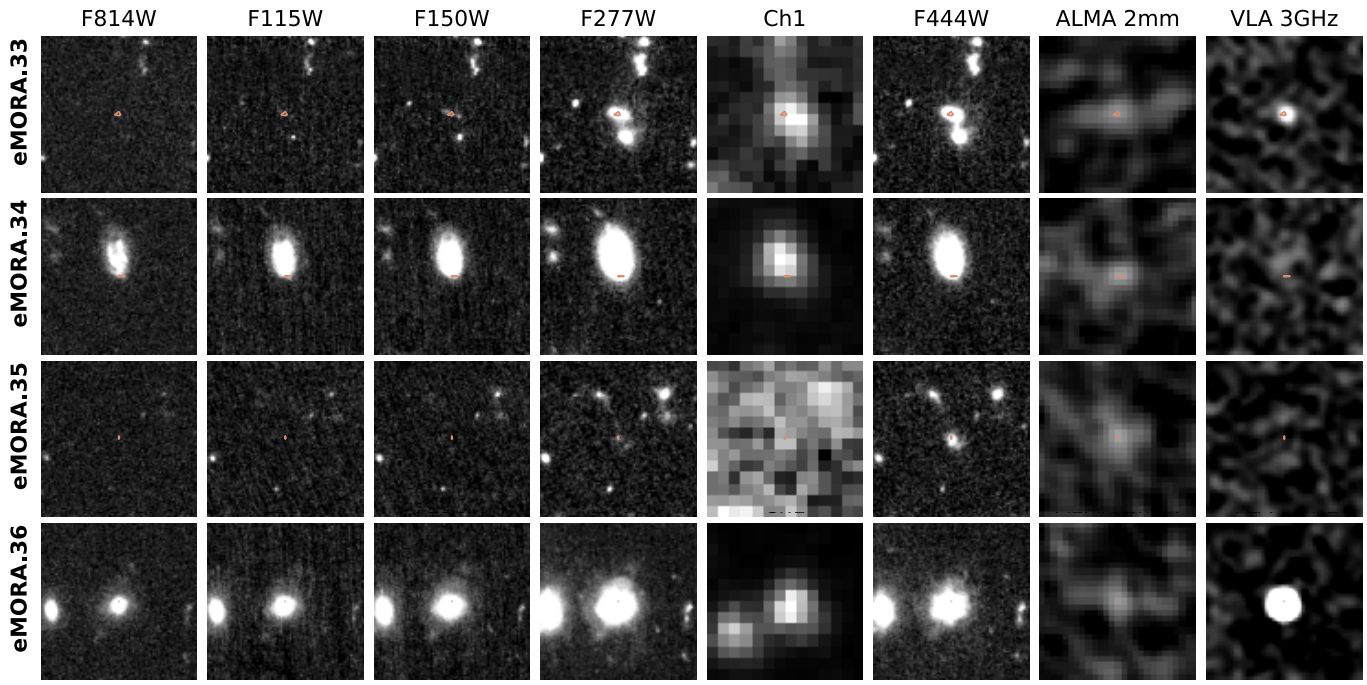

Figure 3. (Continued.)

$z < 1$ radio-boosted sources are also undetected in the SCUBA-2 maps, suggesting that the synchrotron emission is from AGN activity rather than star formation processes. Given that only a small fraction ($n = 2/33$, or $<10\%$) of dust-luminous Ex-MORA galaxies lack submillimeter detections, we conclude that 2 mm follow-up on SCUBA-2 sources may prove an efficient filter for high-z dust-obscured systems, as suggested in O. R. Cooper et al. (2022) and L. L. Cowie et al. (2023).

As in C21 and Z21, we remove the three synchrotron-boosted sources for our statistical analyses of dust continuum emitters, and note that our results presented in Section 4 do not change significantly if these sources were included.

3.4. Source Redshifts

Of the 36 bona fide sources presented herein, 18 have spectroscopic redshifts established in the literature, with 10 at $z_{\rm spec} > 3$. These spectroscopic redshifts are compiled from several catalogs across multiple wavelengths, with the majority compiled in A. A. Khostovan et al. (2025). This includes the following original surveys: rest-frame optical/UV redshifts are from S. J. Lilly et al. (2007), J. R. Trump et al. (2007), M. Kriek et al. (2015), J. P. Stott et al. (2016), T. Nanayakkara et al. (2016), Z. C. Marsan et al. (2017), G. Hasinger et al. (2018), E. Wisnioski et al. (2019), B. Vanderhoof et al. (2026, in preparation), J. Kartaltepe et al. (2026, in preparation), and P. Capak et al. (2026, in preparation); CO-derived redshifts are from M. S. Yun et al. (2015), S. Jin et al. (2019), C. M. Casey et al. (2019), E. F. Jiménez-Andrade et al. (2020), C.-C. Chen et al. (2022), and C.-C. Chen et al. (2026, in preparation). A handful of sources have spectroscopic redshifts based on a single CO transition line, meaning their interpretation could be uncertain. We discuss how we address each of these sources individually in Appendix A.1.

Historically, obtaining photo-zs for dusty galaxies is difficult (C. M. Casey 2020; O. R. Cooper et al. 2022; S. M. Manning et al. 2022), typically driven by a lack of >2–3 UV-to-near-IR detections. Thankfully, in the era of JWST's sensitive near-to-mid-IR imaging at high angular resolutions, this is improving (e.g., S. Gillman et al. 2023; S. M. Manning et al. 2025; J. McKinney et al. 2025). Thus, for the majority of the remaining sources, we use photometric redshifts derived via the BAGPIPES SED-fitting code (A. C. Carnall et al. 2018) using all of the available UV-to-mid-IR photometry as described in Section 3.2. We allow the stellar mass to vary between $10^{6-13}\,M_{\odot}$, and the stellar metallicity from 10^{-3} to $10^{0.4}$, both with log-uniform priors. We adopt a nonparametric star formation history (SFH) model, with five bins in age (fixed bin edges at 10, 30, 100, 300, and 600 Myr) and a constant SFH in each bin. We adopt the "continuity prior," to explicitly weigh against significant SFR changes between adjacent bins and avoid overfitting the data (as described in J. Leja et al. 2019). We include nebular emission, and allow the ionization parameter $\log U$ to vary from –3 to –1. Dust attenuation is included following a D. Calzetti et al. (2000) attenuation law with A_V allowed to vary from 0–6 with a uniform prior.

We compare the calculated photo-zs to spectroscopic redshifts for the 18 available sources in Figure 4 and find good agreement, with a normalized median absolute deviation (NMAD; defined in G. B. Brammer et al. 2008) of $\sigma_{\rm NMAD} = 0.08$. We quantify the catastrophic outlier fraction as the fraction of galaxies with $|z_{\rm phot} - z_{\rm spec}| \geqslant (5 \times \sigma_{\rm NMAD})(1 + z_{\rm spec})$ (see J. R. Weaver et al. 2024, for another example) and find that less than one in five of the photo-zs are $5\sigma_{\rm NMAD}$ away from the one-to-one relation. We also compare newly derived redshifts to those derived in the COSMOS2020 catalog (when available) and find the majority of source redshift estimates are also in similarly good agreement. A precision of $\sigma_{\rm NMAD} = 0.08$ in COSMOS2020 is close to the $\sigma_{\rm NMAD}$ derived for the faintest of i-band detections ($i = 25$–27 AB); this is well in alignment with AB magnitudes for the handful of i-band detections across Ex-MORA galaxies.

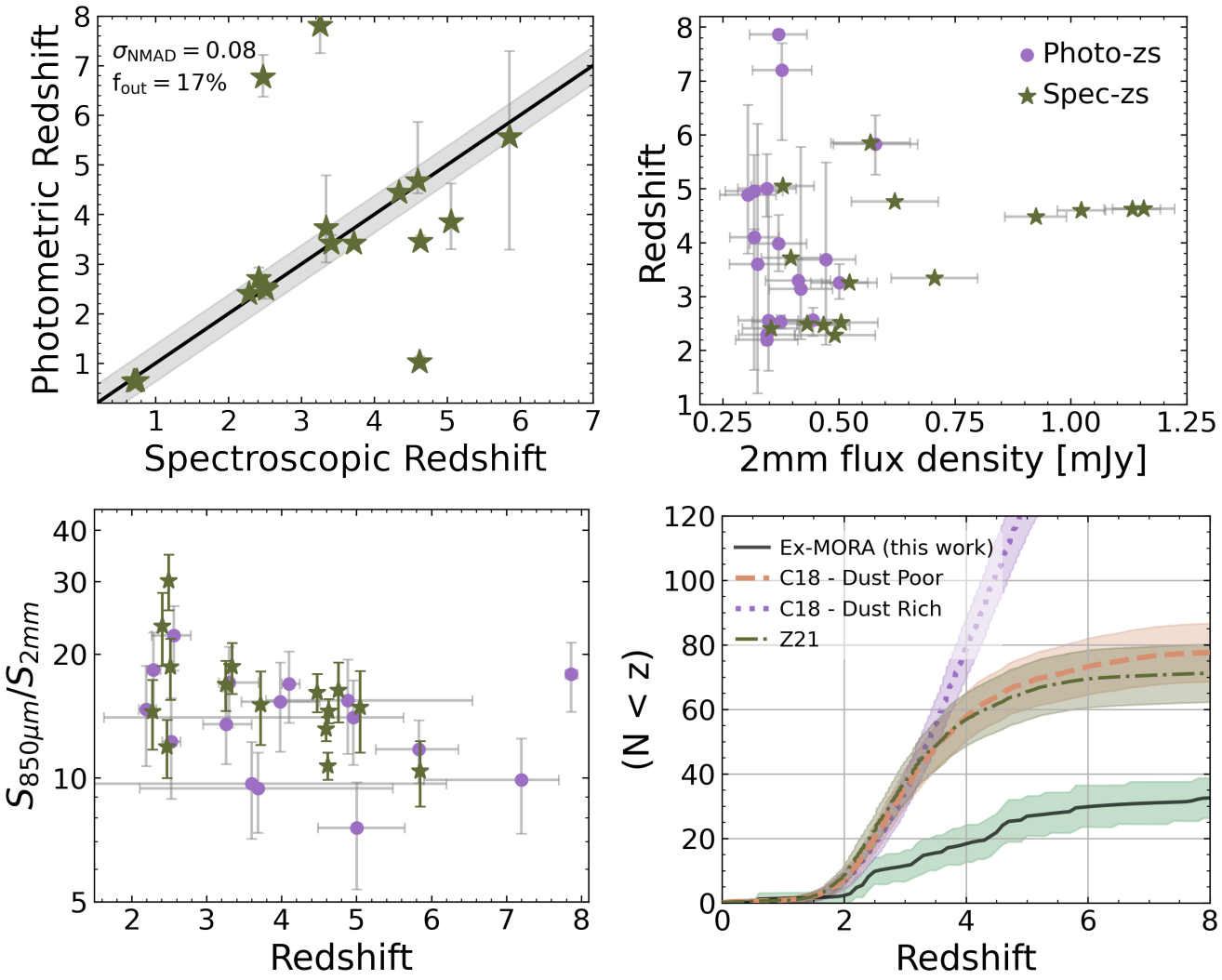

Figure 4. Top-left panel: comparison between spectroscopic redshifts and photometric redshifts for sources with spec-zs from the literature. Solid black line represents the one-to-one relation, the shaded gray region represents the normalized median absolute deviation (NMAD) of the sample (also reported in the top left), and the outlier fraction (defined in Section 4.2) is also reported in the top left. Top-right panel: relationship between 2 mm flux density and source redshifts. Sources with spectroscopic confirmation are represented as green stars, while sources with only photometric redshifts are shown as purple circles. Some of the spectroscopic sources suggest a positive trend between 2 mm flux and source redshift, but the trend is washed out by sources with photo-zs and a few low-flux $z_{spec} \gtrsim 4$ sources. Bottom-left panel: relationship between adopted redshift and $S_{850\ \mu m}/S_{2\ mm}$ flux ratios, as seen in O. R. Cooper et al. (2022) and C21, but only for sources that are thermal dust emitters. Bottom-right panel: the cumulative distribution function (CDF) of source redshifts is shown in dark green, with light green representing the 1σ uncertainty. Results from the original MORA survey (Z21) are shown as a green dashed–dotted line. CDFs from the C. M. Casey et al. (2018a, 2018b) theoretical models representing a "dust-poor" vs. "dust-rich" early Universe are represented as a pink dashed and purple dotted line, respectively.

For posterity, we also compute photo-zs using CIGALE (D. Burgarella et al. 2005; S. Noll et al. 2009; M. Boquien et al. 2019), using similar prescriptions as presented in F. Gentile et al. (2024a) for candidate high-z DSFGs. CIGALE allows for flexible dust attenuation and emission prescriptions, and operates assuming an energy-balance principle such that the energy absorbed by dust in the UV/optical regime is re-emitted in the far-IR. For these fits, we include all available data from UV to far-infrared wavelengths. We note that, as described in Section 3, the vast majority of the sample has at least two points to constrain the far-IR dust blackbody (i.e., SCUBA-2 at 850 μm and ALMA 2 mm), while roughly half of the sample has an additional measurement between 1 and 3 mm. Resulting SEDs are shown in Appendix A.1, Figure 7. We calculate photo-zs and corresponding uncertainties by measuring the median, 16th, and 84th percentiles of the redshift probability distribution.

We calculate average photo-zs for the Ex-MORA galaxy sample by sampling each of their redshift probability distributions 100 times (treating those with spec-zs as delta functions), and then computing the 16th, 50th, and 84th percentiles of the combined samples. In general, we find that CIGALE photo-zs are in agreement with (though slightly higher than) those generated by BAGPIPES, where $\langle z_{\rm CIGALE} \rangle = 4.54^{+2.35}_{-1.95}$ and $\langle z_{\rm BAGPIPES} \rangle = 3.41^{+1.68}_{-1.21}$. When compared to the spectroscopic sample, CIGALE photo-zs overall are slightly poorer than BAGPIPES, with $\sigma_{\rm NMAD} = 0.15$. This may be because BAGPIPES uses a fully Bayesian approach, generating probability distributions for each parameter, enabling a finer detail of SED sampling than the frequentist/grid-based method of CIGALE, which is limited to the granularity of the input parameters. However, the catastrophic outlier fraction for CIGALE is lower at 10%, with all of these outliers being sources with $z_{\rm spec} \sim$ 3–5 for which CIGALE prefers solutions at redshifts $z_{\rm phot} =$ 7–8. This is similar to findings in J. McKinney et al. (2025), where photo-zs

generated using only UV/optical data yielded more accurate redshifts (i.e., smaller $\sigma_{\rm NMAD}$) when compared to the photo-z fits using the panchromatic data (from UV-to-far-IR), and were also on average lower than the latter fits. For comparison, we also computed CIGALE photo-zs using only the UV/optical data, and found that the average redshift drops slightly down to $\langle z\rangle = 4.13^{+2.71}_{-1.88}$. The UV/optical-only CIGALE photo-zs have a similar $\sigma_{\rm NMAD}$ as the multiwavelength fits, but a significantly lower outlier fraction of ∼6% (or one galaxy), hinting again that UV/optical-only fits may be the more conservative choice when modeling DSFGs with multiple UV/optical detections. Given that CIGALE shows a potential tendency to overpredict photo-zs for these galaxies in general, and that the BAGPIPES fits have a lower $\sigma_{\rm NMAD}$, we choose to move forward with the bagpipes photo-zs as the more conservative option.

For three sources (eMORA.20, eMORA.22, and eMORA.23), BAGPIPES produced an unphysically low-z solution, placing them all at $z \sim 1.2$. If true, this would make these sources near HyLIRGS ($L_{\rm IR} \sim 10^{13}\,L_{\odot}$) and, therefore, significantly detected in Herschel SPIRE bands, with $S_{850\,\mu{\rm m}} \gtrsim 50$ mJy (C. M. Casey et al. 2014). All three sources are not detected above 1σ significance in the existing Herschel maps (S. J. Oliver et al. 2012), and therefore, we reject these solutions. Instead, we adopt their CIGALE photo-z estimates. Lastly, BAGPIPES completely failed to fit eMORA.29 (likely due to the unique combination of few detections *and* few upper limits); for this source, we also adopt the CIGALE photo-z estimate. We note that eMORA.11, unlike eMORA.29, has only one UV/optical detection in the F444W band but was still successfully fit by both BAGPIPES and CIGALE; this is likely because of the many more upper limits ($n \sim 10$) provided for this source, which can provide meaningful constraints in the absence of significant detections.

4. Results and Discussion

In the following section, we report statistics on the Ex-MORA sample redshift and 2 mm flux density distributions. We do not include eMORA.31 (the likely spurious source), nor the three synchrotron emitters from these analyses, as the primary goal of this work is to survey thermal dust emission at 2 mm. Still, we stress that the results agree within 1σ uncertainty even if these sources are included.

4.1. 2 mm Cumulative Number Density

The cumulative number density is defined as the on-sky surface density of sources above a certain flux density threshold, per square degree. We derive the cumulative number density in a similar fashion as presented in Z21 using the 5σ source catalog and corresponding completeness and contamination uncertainties, as described at the end of Section 2. We describe this process briefly here. First, we estimate the contribution of a source to the cumulative number density through the following equation:

$$\eta_i(S_i,\,\sigma_i) = \frac{1 - f_{\rm cont}\,(\sigma_i)}{\zeta(S_i) A_{\rm eff}} \tag{1}$$

for a source with a given deboosted flux density, S_i, and SNR, σ_i; $f_{\rm cont}(\sigma_i)$ is the contamination fraction (i.e., fraction of false positives) for the measured SNR (σ_i); $\zeta(S_i)$ is the corresponding completeness for the flux density, and $A_{\rm eff}$ is the area of the Ex-MORA map (577 arcmin^2). Cumulative number counts are calculated as $N(>S) = \Sigma_i \eta_i(S_i,\,\sigma_i)$.

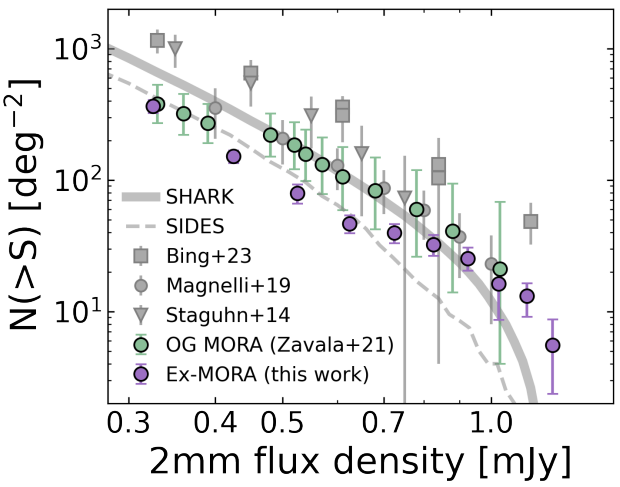

Figure 5. The 2 mm cumulative number density as a function of solid angle. In gray, we collate data from other 2 mm blank-field sky surveys (J. G. Staguhn et al. 2014; B. Magnelli et al. 2019; L. Bing et al. 2023), the SHARK simulation (C. d. P. Lagos et al. 2020), and the SIDES simulation (M. Béthermin et al. 2017). Measurements from the original (OG) MORA survey derived in Z21 are presented as light-green circles, and measurements from the Ex-MORA Survey (this work) are presented as purple circles.

In order to propagate flux, completeness, and contamination uncertainties into the cumulative number densities, we generate a Monte Carlo simulation. For each iteration, we model individual source flux densities as a Gaussian distribution, setting the dispersion equal to the measured uncertainty. We sample the respective distribution for each individual source and recalculate the SNR given the local noise around that source. We then use this SNR to sample the contamination fraction (which was generated as a function of SNR, as described in Section 2, and modeled as Gaussians). Each individual source in each iteration also has its own completeness estimates, based on the artificial source injection simulations mentioned in Section 2 and in Z21. We repeat this process 10^3 times, each time calculating the resulting cumulative number density and corresponding Poisson noise over flux density bins of size 100 μJy. We then calculate the mean, 16th, and 84th percentiles, and average Poisson noise in each flux density bin. The resulting cumulative number density is shown in Figure 5, and reported in Table 3. We repeat the above processes while including the four removed sources and find that the differences between cumulative number densities is not significant, and within the uncertainty of the "cleaned" cumulative number density. These are also presented in Table 3.

In Figure 5, we compare our results to existing 2 mm number counts from blank-field surveys across the literature: the 31 arcmin^2 and 250 arcmin^2 GISMO/IRAM surveys reported in J. G. Staguhn et al. (2014) and B. Magnelli et al. (2019), respectively; the 1010 arcmin^2 COSMOS portion of the IRAM NIKA2 Cosmological Legacy Survey (L. Bing et al. 2023); the number counts from the original MORA survey in Z21; and predictions from the SHARK (C. d. P. Lagos et al. 2020) and SIDES (M. Béthermin et al. 2017) cosmological simulations. On average, all literature estimates are greater than those we calculate by a factor of 2–3, with the exception of the NIKA2-CLS COSMOS estimates, which are 7×–8× higher than our estimates. The NIKA2-CLS cumulative number densities shown in Figure 5 are the *source* counts, not the galaxy counts. Due to

Table 3
Ex-MORA 2 mm Cumulative Number Densities

$S_{2\,\mathrm{mm}}$ (mJy)	All Sources			Cleaned Sample		
	$N(>S)$ (deg^{-2})	$-\delta N$ (deg^{-2})	$+\delta N$ (deg^{-2})	$N(>S)$ (deg^{-2})	$-\delta N$ (deg^{-2})	$+\delta N$ (deg^{-2})
0.30	365	42	41	325	36	38
0.40	152	17	16	134	16	15
0.50	79	13	13	72	13	12
0.60	47	7	7	39	7	6
0.70	40	7	7	32	6	6
0.80	32	6	6	25	5	5
0.90	25	5	5	25	5	5
1.00	16	8	7	16	8	7
1.10	13	4	3	13	4	3
1.20	6	3	3	6	3	3

Note. The "Cleaned Sample" corresponds to Figure 5 and represents estimates with the spurious source (eMORA.31) and significant synchrotron emitters (eMORA.5, eMORA.15, and eMORA.36) removed.

the large beam size of single-dish NIKA2 at 2 mm (18"), true galaxy sources are expected to blend together (M. Béthermin et al. 2017). We apply the "source-to-galaxy counts correction factor" derived for this survey in L. Bing et al. (2023) and find that our estimates are in better agreement, within a factor of ∼2, which is similar to the other estimates reported in the literature. Finally, we note that the SHARK semianalytical model is roughly successful (within uncertainty) in predicting number densities at $S_{2\,\mathrm{mm}} \gtrsim 800\,\mu$Jy, but then overpredicts the faint end by ∼2σ–3σ. The SIDES model, however, performs in an opposite manner, better modeling the observed cumulative number densities at $S_{2\,\mathrm{mm}} \lesssim 700\,\mu$Jy, but not quite meeting the bright end. We also note that SHARK produces overall more 2 mm luminous sources per Mpc^3 than SIDES (and Ex-MORA), which likely produces the systemic offset between the two simulations. As mentioned in C21, some of the differences in alignment with the observations may be driven by intrinsic differences in the redshift distributions of the 2 mm population. For example, for sources with $S_{2\,\mathrm{mm}} >= 300\,\mu$Jy (like Ex-MORA), both simulations produce average redshifts around ∼3.2, which is slightly lower than our survey results (∼3.6). SIDES predicts that higher redshifts correlate with higher 2 mm fluxes (which may be supported by the Ex-MORA sample; see Figure 4 and Section 4.2), and therefore, Ex-MORA's slightly higher-redshift distribution may drive divergence from the SIDES model at the bright end.

We note a distinct difference between the number density shapes/distributions between Ex-MORA and the original MORA survey (Z21). By eye, the MORA cumulative number densities appear to follow a Schechter function, while the Ex-MORA cumulative number densities appear more like a double Schechter function, as Ex-MORA has an apparent comparative deficit in sources with flux densities between 400 and 800 μJy (though the surveys only differ beyond 1σ uncertainty at 400–600 μJy). We tested whether these differences could be driven by potential variances in data reduction techniques, beam sizes, and/or weather, and find no significant changes in our resulting sample size/cumulative number density. It is possible that completeness corrections for sources at $S_{2\,\mathrm{mm}} \lesssim 700\,\mu$Jy in the original MORA survey were somewhat overestimated, as MORA had overall poorer rms (with only ∼60% of the map with an rms of 90 $\mu\mathrm{Jy\,beam}^{-1}$ or less, versus 90% for the Ex-MORA map; see Figure 2), resulting in low source recovery for fainter sources in the source injection simulations. Ex-MORA, being both deeper and wider, had only significant completeness corrections for sources with flux densities $\lesssim$450 μJy, which corresponds to the 5σ threshold for a map with rms (σ) = 90 $\mu\mathrm{Jy\,beam}^{-1}$. For MORA, the corresponding 90% rms is ∼156 $\mu\mathrm{Jy\,beam}^{-1}$, setting the 5$\sigma$ threshold at 780 μJy, which is near where we begin to see the departure between survey results as the completeness corrections in MORA become significant (>10%). Both surveys estimate the same number of sources at the faintest end (within uncertainty), where $S_{2\,\mathrm{mm}} \sim 300\,\mu$Jy, which, at 5$\sigma$, corresponds to an rms of 60 $\mu\mathrm{Jy\,beam}^{-1}$. While the rms varies over both maps and Ex-MORA is generally deeper, both Ex-MORA and MORA have a small fraction of the map at or below an rms of 60 $\mu\mathrm{Jy\,beam}^{-1}$ (∼2%–6%), which means that the completeness corrections for sources near this flux density are likely similar across both surveys.

4.2. Redshift Distribution of 2 mm Sources

In Figure 4, we present the cumulative distribution function (CDF) of Ex-MORA sources. We calculate the CDF over 10^3 iterations. For each instance, we sample from each source's redshift probability distribution function (PDF), $p(z)$, for galaxies with photo-zs, while galaxies with spec-zs are treated as delta functions. We then calculate the mean CDF and 68% confidence interval from the 10^3 CDFs generated in the 10^3 iterations.

Based on the CDF, we find that 93^{+3}_{-4}% of 2 mm selected sources are at $z > 2$, 65^{+3}_{-3}% at $z > 3$, and 44^{+4}_{-4}% at $z > 4$. This means that most 2 mm selected sources are likely at $z > 3$, and nearly *half* are likely at $z > 4$. We sample from the CDF and corresponding uncertainties to measure a median redshift of $\langle z\rangle = 3.8^{+1.7}_{-1.52}$, which is remarkably equivalent to the estimate derived in C21 over a smaller area using less sensitive OIR data. This average is higher than the smaller and shallower GISMO/IRAM 2 mm Survey in J. G. Staguhn et al. (2014; $z \sim 3$), but is in better agreement with the average found in the corresponding follow-up survey that is ∼8× larger in area than the original (B. Magnelli et al. 2019), with $\langle z\rangle = 3.9$.

In Figure 4, we also show redshift CDFs from the C. M. Casey et al. (2018a, 2018b) theoretical models representing a "dust-poor" versus "dust-rich" early Universe. In this scenario, a "dust-poor" early Universe is one without intense, dusty starbursts (with obscured SFRs $> 100\,M_\odot\,\mathrm{yr}^{-1}$), *not* an early Universe devoid of galaxies with significant fractions of obscured star formation (see, e.g., Y. Fudamoto et al. 2020; H. S. B. Algera et al. 2023). The models are generated by sampling over a simulated 2 mm survey of the same on-sky area as Ex-MORA. While the Ex-MORA survey is successful at identifying primarily $z > 3$ IR luminous galaxies, the results are still consistent with—and even markedly below—the "dust-poor" model. This means that the number density of heavily obscured, starbursting galaxies at high-z should decrease with increasing redshift at $z > 3$, and that the cosmic SFR density may be less dominated by extreme systems of obscured star formation during these epochs. The former implication is demonstrated in Section 4.3, while the latter will be presented in a forthcoming paper. Combining cumulative number densities from the original MORA survey with 1.2 and 3 mm number counts from the literature, Z21 generated an independent prediction for the cumulative

redshift distribution of 2 mm selected sources,[44] predicting roughly twice the number of $z > 3$ sources than what we measure, even though their predictions are also consistent with a "dust-poor" early Universe. They estimated that the evolution of the characteristic number density of IR luminous galaxies $\Phi_\star \propto (1+z)^\psi$ is steeply declining at $z \gtrsim 2$, with $\psi = -6.5^{+0.8}_{-1.8}$. Given that Ex-MORA produces even fewer 2 mm luminous galaxies at $z > 3$ than expected based on the model in Z21, it is likely that $\Phi_\star$ is declining at an even more rapid rate, with $\psi < -6.5$. Future work using Ex-MORA to constrain the evolution of the IR luminosity function parameters at higher detail will be forthcoming.

We also explore the relationship between source redshifts and their 2 mm flux densities, as well as their ratios between 850 μm and 2 mm flux densities, in Figure 4. This latter ratio was shown to potentially correlate with source redshifts such that lower ratios correspond to higher redshifts as the 850 μm and 2 mm bands begin mutually probing the peak of dust emission (C. M. Casey et al. 2021; O. R. Cooper et al. 2022). As can be seen in C. M. Casey et al. (2021) and O.R. Cooper et al. (2022), both relationships show potential for correlation such that higher-redshift sources are on average brighter at 2 mm, and have lower $S_{850\,\mu\mathrm{m}}/S_{2\,\mathrm{mm}}$ ratios. This appears particularly true for most of the spectroscopically confirmed sources in the Ex-MORA sample. However, when considering sources with photometrically derived redshifts, both of these trends appear to wash out. Future follow-up spectroscopic surveys over larger samples will prove fruitful in ascertaining whether these values are truly correlated with galaxy redshifts at $z \gtrsim 3$.

4.3. Volume Density of 2 mm Sources at z $\gtrsim$ 3

The large contiguous area of the Ex-MORA survey, combined with rich ancillary data (including JWST imaging) and a well-defined flux threshold, enables strong constraints on high-z DSFG volume densities. In Figure 6, we present the volume density of Ex-MORA sources over $z = 0$–8 alongside estimates collated from the literature using a variety of DSFG samples (M. J. Michałowski et al. 2017; C. C. Williams et al. 2019; C. d. P. Lagos et al. 2020; F. Valentino et al. 2020; C.-C. Chen et al. 2022; S. M. Manning et al. 2022). We calculate our estimates using the same method presented in Section 4.2 in volumes encompassed by redshift bins of size $\delta z = 1$ over the Ex-MORA survey area. We add in quadrature cosmic variance, σ_{CV}, over the various redshift bins following the prescription in J. McKinney et al. (2026, in preparation) using the standard assumptions and cookbook presented in B. P. Moster et al. (2011). We note that σ_{CV} dominates the volume density uncertainties for 2 mm luminous sources at $z > 2$. The resulting calculations and corresponding uncertainties are presented in Table 4.

Current volume density estimates of submillimeter-luminous DSFGs at $z \gtrsim 3$ are in tension by a factor of ~100, ranging from $\sim 3 \times 10^{-5}\,\mathrm{Mpc}^{-3}$ (C. C. Williams et al. 2019) to $\sim 4 \times 10^{-7}\,\mathrm{Mpc}^{-3}$ (F. Valentino et al. 2020, 2023). In this sample, we derive a roughly steady volume density of 2 mm bright galaxies from $z = 2$ to 6 of ~ 3–$5 \times 10^{-6}\,\mathrm{Mpc}^{-3}$, with a total $z > 3$ volume density of 1–3 $\times 10^{-5}\,\mathrm{Mpc}^{-3}$. These estimates agree well with measurements derived from hundreds of SCUBA-2 selected DSFGs in M. J. Michałowski et al. (2017), but they are slightly higher (specifically at $z > 3$) than the (duty cycle corrected) volume densities reported in C.-C. Chen et al. (2022). However, the latter study at present has a much smaller sample size. We also compare to the SHARK (C. d. P. Lagos et al. 2020) and SIDES (M. Béthermin et al. 2017) cosmological models by only including sources with $S_{2\,\mathrm{mm}} > 300\,\mu$Jy (the lower flux density threshold of our sample). Despite general success in modeling the bright end of the 2 mm cumulative number density, both models overpredict the abundance of 2 mm sources across $z \sim 2$–4 by roughly a factor of 3; however, the models do exhibit a similar rate of population decrease from $z = 4$ to $z = 7$, and are in better agreement with the observed number densities at $z > 4$. We note that, while we include number density estimates for $z = 7$–9 DSFGs, these are highly uncertain due to small sample sizes, large cosmic variance, and photo-z uncertainties at these epochs. Thus, we do not compare these estimates to simulations and urge the reader to interpret with caution until spectroscopic confirmation across the Ex-MORA sample.

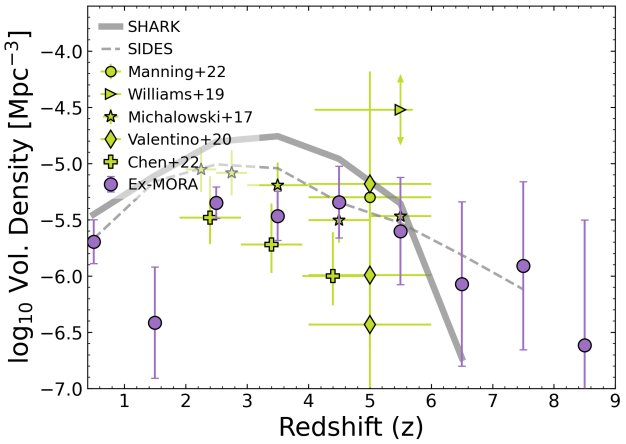

Figure 6. The estimated volume density evolution of 2 mm sources in the Ex-MORA Survey is shown as purple dots, with corresponding values listed in Table 4. Comparative studies on DSFG number densities using a variety of other selection techniques/wavelengths are delineated in green (M. J. Michałowski et al. 2017; C. C. Williams et al. 2019; F. Valentino et al. 2020; C.-C. Chen et al. 2022; S. M. Manning et al. 2022). We also show estimates of 2 mm bright sources ($S_{2\,\mathrm{mm}} >= 0.3$ mJy) from the SHARK (C. d. P. Lagos et al. 2020) and SIDES (M. Béthermin et al. 2017) in gray.

Table 4
Ex-MORA 2 mm Volume Densities

Redshift	$\log_{10}(n/\mathrm{Mpc}^{-3})$	σ_{CV}
$0 < z < 1$	-5.68 ± 0.2	0.09
$1 < z < 2$	-6.43 ± 0.50	0.09
$2 < z < 3$	-5.35 ± 0.14	0.13
$3 < z < 4$	-5.48 ± 0.22	0.20
$4 < z < 5$	-5.35 ± 0.32	0.31
$5 < z < 6$	-5.59 ± 0.48	0.46
$6 < z < 7$	-6.07 ± 0.72	0.64
$7 < z < 8$	-5.91 ± 0.67	0.72
$8 < z < 9$	-6.62 ± 0.97	0.81

4.4. Other High-z Red Selection Techniques

In recent years, several new techniques were developed to efficiently select $z > 3$ dusty galaxies, with a special focus on

[44] We note that, while Z21 uses MORA number counts to generate their predictions, the combination of other wavelengths and the methods employed therein make their predictions independent from those derived from direct source characterization, as done in this work. See C21 for more details.

sources with faint or no emission at OIR wavelengths. These "OIR-dark" galaxies are believed to live predominantly at high redshifts ($z > 3$), contribute significantly to the cosmic SFR density (∼10%–50%), and serve as a primary parent population for the first massive quiescent galaxies at $z \sim 3$–5 (T. Wang et al. 2019; M. Talia et al. 2021; A. Enia et al. 2022; S. M. Manning et al. 2022; L. Barrufet et al. 2023; D. van der Vlugt et al. 2023; M. Y. Xiao et al. 2023, 2023b). It is important to note, however, that each of these methods selects different populations of dusty galaxies (e.g., Section 5.2 in M. Talia et al. 2021), with variations over average SFRs, stellar masses, and redshifts. In the following, we apply some of these techniques to the Ex-MORA sample to understand how this population may or may not be included in such studies.

We first apply the radio + OIR-dark selection technique defined in F. Gentile et al. (2024a). This selection technique requires that galaxies have 3 GHz flux densities >12.65 μJy and do not have a detection in COSMOS2020 (J. R. Weaver et al. 2022); the reddest band used for source detection in COSMOS2020 is the UltraVISTA K_s filter ($\lambda \sim 2.2$ μm) with a 3σ limiting depth at $m_{\rm AB} \sim 25.5$. We find that 22/36 (∼60%) sources have sufficiently bright 3 GHz emission (>12.65 μJy) to pass the first selection criterion, though three sources are known AGN and, thus, should be removed from this sample. Out of the remaining 19 Ex-MORA galaxies, only three sources are sufficiently faint to have no counterpart in the COSMOS2020 catalog. If we instead use the F277W band as a proxy for the K_s band (with the 3σ magnitude limit mentioned above), we only recover one source, with the other two becoming slightly too bright to be captured.

We next apply the OIR-dark selection technique defined in T. Wang et al. (2019) but updated using JWST NIRCam filters (L. Barrufet et al. 2023; R. Gottumukkala et al. 2024). The OIR-dark selection technique, when used with JWST bands, requires F150W − F444W > 2.1 and a faint or nondetection in the F150W band ($m_{\rm F150W} > 25$). We find that a little under half ($n = 14/33$) of Ex-MORA sources would be captured with this technique. Of the sources not captured: most have sufficiently red F150W − F444W colors to meet the first criterion (F150W − F444W > 2.1), but their F150W magnitudes are too bright (<25 mag). We note that *all* of the sources captured by this technique are undetected in the F150W band; given the observational depths of the F150W band in the COSMOS-Web survey ($m_{\rm AB} \lesssim 27$; C. M. Casey et al. 2023), it is likely that that these sources are truly "dark." Sources without F150W detections have an average redshift of $z \sim 4.4$, while those with F150W detections sit near $z \sim 3.3$ (though these averages are at the edge of 1σ uncertainty of one another).

Combined, it seems that these optical/near-IR and radio selection techniques capture roughly 10%–40% of all 2 mm bright sources, supporting the idea that the heavily dust-obscured population is quite heterogeneous. The population densities derived using these methods are similar to our estimates when considering all Ex-MORA sources at $z > 3$ (~ 1–3×10^{-5} Mpc^{-3}; M. Talia et al. 2021; M. Y. Xiao et al. 2023), yet there is little to no overlap between sources identified via these three methods. This is particularly troubling, as it implies that up to two-thirds of the $z > 3$ dusty galaxy population is missed when using only one of these selection techniques (and there may be more dust covered SFR in galaxies at these epochs than previously thought; e.g., H. S. B. Algera et al. 2023; D. T. Zimmerman et al. 2024). If confirmed, the consequences of such biases are wide-sweeping, affecting theories and estimates on early and rapid metal enrichment of the interstellar medium, the dust-obscured component of the cosmic SFR density, and early massive quiescent galaxy progenitor populations. This also implies that compiling the most complete samples of DSFGs at high-z requires a combination of observations across several energy regimes, further solidifying how synergies between major observing facilities such as JWST and ALMA are critical to this aim.

5. Summary and Conclusions

We have presented the Ex-MORA Survey, the largest ALMA blank-field map covering 577 arcmin^2 at 2 mm. This work is an expansion on the original MORA survey presented in Z21 and C21. We detect 37 sources above 5σ significance, one of which is likely a false positive, and three of which likely have 2 mm fluxes boosted significantly by synchrotron emission, leaving a total of 33 robust detections from predominantly thermal dust emission. All bona fide sources are detected at minimum in the NIRCam F444W band.

Through a combination of spectroscopic and photometric redshifts spanning $z \sim 2$–8, we estimate a median redshift of $\langle z \rangle = 3.8^{+1.7}_{-1.52}$. Two-thirds of the sample are estimated at $z > 3$, and just under half of the sample is estimated at $z > 4$. We estimate the volume density of Ex-MORA sources and measure a decrease in the population from $z \sim 4$ to $z \sim 7$, with a total integrated volume density of ~ 1–3×10^{-5} Mpc^{-3} at $z > 3$. In upcoming work, we will present the physical properties of individual Ex-MORA sources and explore them in the context of galaxy evolution paradigms.

While the Ex-MORA survey is successful at identifying a strong sample of primarily $z > 3$ IR luminous galaxies, the results are still consistent with the "dust-poor" early Universe model presented in C. M. Casey et al. (2018a). At face value, this implies that searches for high-z heavily dust-obscured galaxies will become more difficult with increasing redshift, as these sources are incredibly rare (though known to exist; e.g., D. P. Marrone et al. 2018; J. A. Zavala et al. 2018b; H. B. Akins et al. 2023; A. P. S. Hygate et al. 2023). In this work, we find that other techniques developed to discover $z > 3$ dusty galaxies (e.g., T. Wang et al. 2019; M. Talia et al. 2021; L. Barrufet et al. 2023; R. Gottumukkala et al. 2024) capture as much as 40% and as little as 10% of the Ex-MORA galaxy sample. These findings support the idea that multiple modes of selection across multiple wavelengths and energy regimes are necessary for a complete census of the high-z dusty galaxy population, and that synergistic efforts with observatories such as JWST, ALMA, and the VLA will continue to be critical to these efforts.

Acknowledgments

We honor the invaluable labor of the maintenance and clerical staff at our institutions, whose contributions make our scientific discoveries a reality. This work was developed and written in central Texas on the lands of the Tonkawa, Comanche, and Apache people. Learn more about the history and present life of Austin's Indigenous peoples at https://www.kut.org/texas/2022-03-31/where-have-austins-indigenous-people-gone.

A.S.L. thanks Charlie and Patrick Long for the love, support, and precious moments baking in the Sun together. A. S.L. would also like to thank the good people at NRAO Charlottesville for their help in staging and reducing this data, for sharing remote computing resources, for the ALMA Ambassador Program, and for the Visitor Support Program. Specifically, we thank G. Privon, S. Wood, and L. Barcos-Munoz. A.S.L. would also like to thank the LUMA, VanguardSTEM, Black in Astro, and AAS CSMA organizations for providing community and support, with special thanks to A. Harriot, G. Ezeka, M. Sgouros, K. Klass, R. McNair, L. Valencia, A. Walker, N. Cabrera Salazar, and J. Gonzalez Quiles.

A.S.L. and S.M.M. acknowledge support for this work provided by NASA through the NASA Hubble Fellowship Program grant Nos. HST-HF2-51511 and HST-HF2-51484, awarded by the Space Telescope Science Institute, which is operated by the Association of Universities for Research in Astronomy, Inc., for NASA, under contract NAS5-26555. J.H. acknowledges support from the ERC Consolidator Grant 101088676 ("VOYAJ"). J.A.Z. acknowledges funding from JSPS KAKENHI grant No. KG23K13150. F.G. acknowledges the support from grant PRIN MIUR 2017-20173ML3WW_001 "Opening the ALMA window on the cosmic evolution of gas, stars, and supermassive black holes." E.T. acknowledges support from ANID Basal program FB210003 (CATA) and FONDECYT Regular 1190818 and 1200495. J.B.C. acknowledges funding from the JWST Arizona/Steward Postdoc in Early galaxies and Reionization (JASPER) Scholar contract at the University of Arizona. A.W.S.M. acknowledges the support of the Natural Sciences and Engineering Research Council of Canada (NSERC) through grant reference No. RGPIN-2021-03046. M.A. acknowledges support from the ANID BASAL project FB210003

The National Radio Astronomy Observatory is a facility of the National Science Foundation operated under cooperative agreement by Associated Universities, Inc. ALMA is a partnership of ESO (representing its member states), NSF (USA) and NINS (Japan), together with NRC (Canada), MOST and ASIAA (Taiwan), and KASI (Republic of Korea), in cooperation with the Republic of Chile. The Joint ALMA Observatory is operated by ESO, AUI/NRAO, and NAOJ. This work is based [in part] on observations made with the NASA/ESA/CSA JWST. The data were obtained from the Mikulski Archive for Space Telescopes at the Space Telescope Science Institute, which is operated by the Association of Universities for Research in Astronomy, Inc., under NASA contract NAS 5-03127 for JWST. These observations are associated with program JWST Nos. 1727 and 1837. Some of the data presented in this paper are available on the Mikulski Archive for Space Telescopes (MAST) at the Space Telescope Science Institute. The specific observations can be accessed via doi:10.17909/qhb4-fy92 and doi:10.17909/T94S3X. This work made use of Astropy:[46] a community-developed core Python package and an ecosystem of tools and resources for astronomy (Astropy Collaboration et al. 2013, 2018, 2022).

Appendix
Individual Source Redshift Solutions

A.1. Approaching Degenerate Source Spectroscopic Redshifts

A handful of Ex-MORA sources have spectroscopic redshifts generated from a single CO emission line. Without a second line detection (from, e.g., a higher or lower *J*-transition, [C I] or [C II]), interpretation of the corresponding spectroscopic redshift is degenerate across discrete redshift values (see, e.g., S. Jin et al. 2024). We discuss the handful of sources for which this degeneracy is possible, and how we decided which redshift to report.

For two objects (eMORA.7 and eMORA.12), the detected line is attributed to a CO (3–2) transition line, placing these sources at $z \sim 2.31$ and 2.26, respectively. However, given the spectral coverage of the observations (ALMA band 3 only; PID:2019.1.01600.S and 2021.1.00246.S), it is possible to have a single line detection also at CO (4–3), which would place these objects instead at $z \sim 3.34$ and 3.41, respectively. Indeed, the photometric redshifts developed in this work support a $z > 3$ solution for both of these sources, and this agrees with the CO(4–3) redshift within 1σ uncertainty and $\int_3^\infty p(z) > 85\%$. Thus, for these two sources, we adopt the $z \sim 3$–4 solutions in this work.

Another source (eMORA.24) is similar to the above two sources (a single detection reported as CO(3–2) and a corresponding $z < 3$ redshift estimate in C.-C. Chen et al. 2026, in preparation); however, the photo-z estimates strongly agree with the predicted spectroscopic redshift at $z = 2.411$ within 1σ (and $\int_3^\infty p(z) < 5\%$). For this source, we adopt the reported spectroscopic redshift of 2.411.

Finally, one source (eMORA.4) has a single line detection attributed to CO(4–3) with a corresponding redshift of $z = 3.254$. The estimated photo-z from this work is high, at $z \sim 7.8$. If true, this would require a CO(8–7) emission line *and* have a much higher likelihood of detecting multiple *J*-transition lines because (a) the distance between rest-frame wavelengths of CO emission lines becomes smaller with increasing *J*-transitions; and (b) emission-line brightness increases with increasing *J*-transitions. Thus, we reject the high-z photometrically derived solution and adopt its redshift as $z = 3.254$.

In Figure 7, we show panchromatic SEDs of Ex-MORA galaxies. This includes both the CIGALE and BAGPIPES SEDs, and corresponding photo-zs.

[46] http://www.astropy.org

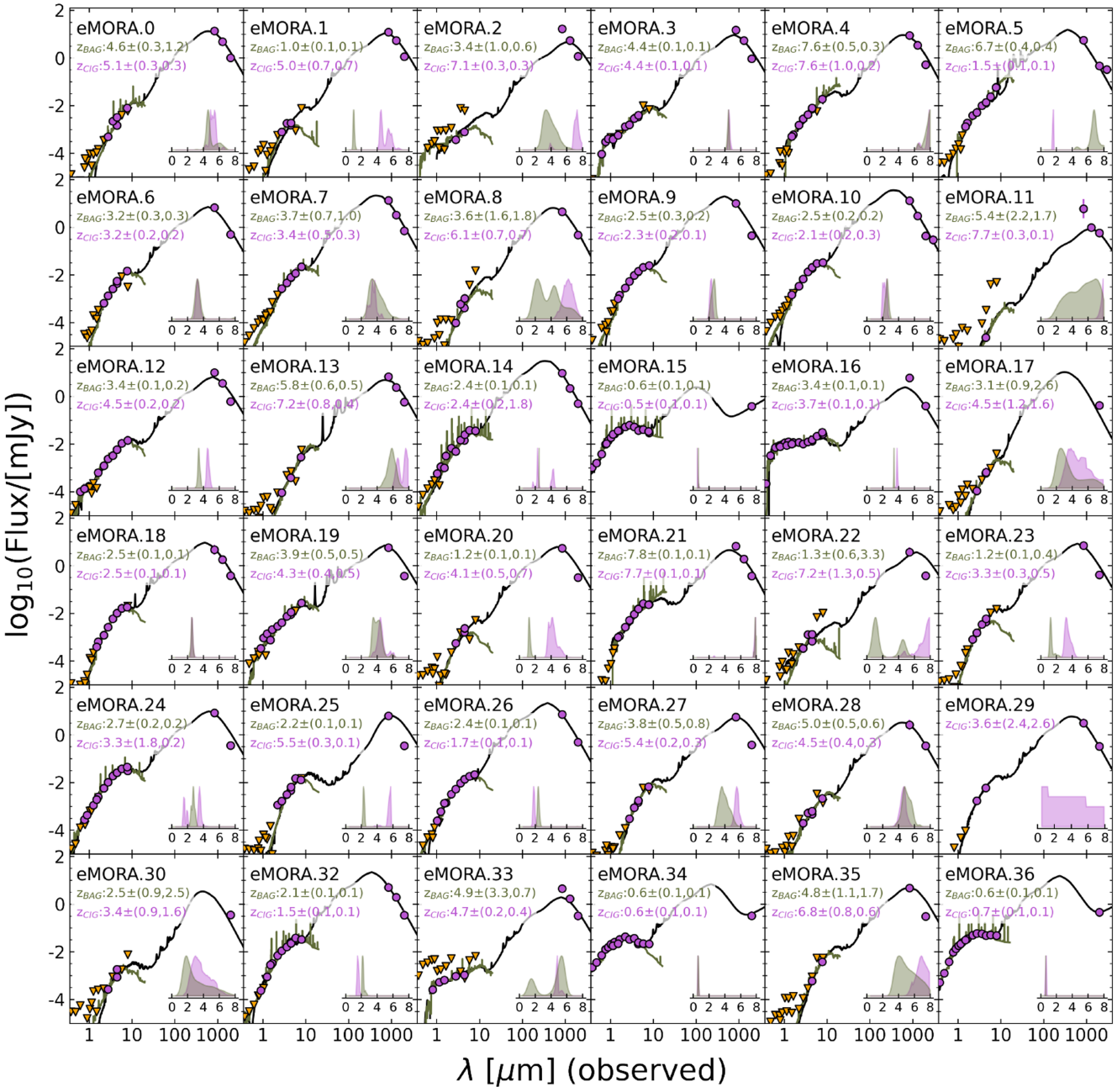

Figure 7. Multiwavelength SEDs fit using CIGALE (black) and BAGPIPES (green) over the Ex-MORA sample, with photo-z probability distribution functions (PDFs) inlaid (purple for CIGALE, green for BAGPIPES). With CIGALE, we use data from UV/optical to millimeter wavelengths, whereas the BAGPIPES fits use only UV/optical data. While full multiwavelength fits may be better for accurately constraining galaxy physical properties (by, e.g., accounting for dust attenuation in the stellar spectrum), the derived photo-zs are on average slightly higher than those derived using only the UV/optical data. This is similar to results found in J. McKinney et al. (2025), and also consistent with CIGALE runs using only the UV/optical data.

ORCID iDs

Arianna S. Long https://orcid.org/0000-0002-7530-8857
Caitlin M. Casey https://orcid.org/0000-0002-0930-6466
Jed McKinney https://orcid.org/0000-0002-6149-8178
Jorge A. Zavala https://orcid.org/0000-0002-7051-1100
Olivia R. Cooper https://orcid.org/0000-0003-3881-1397
Erini L. Lambrides https://orcid.org/0000-0003-3216-7190
Maximilien Franco https://orcid.org/0000-0002-3560-8599
Manuel Aravena https://orcid.org/0000-0002-6290-3198
Matthieu Bethermin https://orcid.org/0000-0002-3915-2015
Karina Caputi https://orcid.org/0000-0001-8183-1460
Jaclyn B. Champagne https://orcid.org/0000-0002-6184-9097
D. L. Clements https://orcid.org/0000-0002-9548-5033
Elisabete da Cunha https://orcid.org/0000-0001-9759-4797
Andreas L. Faisst https://orcid.org/0000-0002-9382-9832
Fabrizio Gentile https://orcid.org/0000-0002-8008-9871
Jacqueline Hodge https://orcid.org/0000-0001-6586-8845
Allison W. S. Man https://orcid.org/0000-0003-2475-124X
Sinclaire M. Manning https://orcid.org/0000-0003-0415-0121
David B. Sanders https://orcid.org/0000-0002-1233-9998
Margherita Talia https://orcid.org/0000-0003-4352-2063

Ezequiel Treister https://orcid.org/0000-0001-7568-6412
Gabriel Brammer https://orcid.org/0000-0003-2680-005X
Marcella Brusa https://orcid.org/0000-0002-5059-6848
Steven L. Finkelstein https://orcid.org/0000-0001-8519-1130
Seiji Fujimoto https://orcid.org/0000-0001-7201-5066
Christopher C. Hayward https://orcid.org/0000-0003-4073-3236
Olivier Ilbert https://orcid.org/0000-0002-7303-4397
Jean-Baptiste Jolly https://orcid.org/0000-0002-3405-5646
Jeyhan S. Kartaltepe https://orcid.org/0000-0001-9187-3605
Kirsten Knudsen https://orcid.org/0000-0002-7821-8873
Anton M. Koekemoer https://orcid.org/0000-0002-6610-2048
Daizhong Liu https://orcid.org/0000-0001-9773-7479
Georgios Magdis https://orcid.org/0000-0002-4872-2294
Henry Joy McCracken https://orcid.org/0000-0002-9489-7765
Jason Rhodes https://orcid.org/0000-0002-4485-8549
Brant E. Robertson https://orcid.org/0000-0002-4271-0364
Nick Scoville https://orcid.org/0000-0002-0438-3323
Kartik Sheth https://orcid.org/0000-0002-5496-4118
Vernesa Smolcic https://orcid.org/0000-0002-3893-8614
Justin Spilker https://orcid.org/0000-0003-3256-5615
Yoshiaki Taniguchi https://orcid.org/0000-0003-2247-3741
Sune Toft https://orcid.org/0000-0003-3631-7176
C. Megan Urry https://orcid.org/0000-0002-0745-9792
Min Yun https://orcid.org/0000-0001-7095-7543

References

Aihara, H., AlSayyad, Y., Ando, M., et al. 2022, PASJ, 74, 247
Akins, H. B., Casey, C. M., Allen, N., et al. 2023, ApJ, 956, 61
Algera, H. S. B., Inami, H., Oesch, P. A., et al. 2023, MNRAS, 518, 6142
Ashby, M. L. N., Willner, S. P., Fazio, G. G., et al. 2015, ApJS, 218, 33
Astropy Collaboration, Price-Whelan, A. M., Lim, P. L., et al. 2022, ApJ, 935, 167
Astropy Collaboration, Price-Whelan, A. M., Sipőcz, B. M., et al. 2018, AJ, 156, 123
Astropy Collaboration, Robitaille, T. P., Tollerud, E. J., et al. 2013, A&A, 558, A33
Bagley, M. B., Finkelstein, S. L., Koekemoer, A. M., et al. 2023, ApJL, 946, L12
Barrufet, L., Oesch, P. A., Weibel, A., et al. 2023, MNRAS, 522, 449
Bassini, L., Feldmann, R., Gensior, J., et al. 2023, MNRAS, 525, 5388
Bertin, E., & Arnouts, S. 1996, A&AS, 117, 393
Béthermin, M., Wu, H.-Y., Lagache, G., et al. 2017, A&A, 607, A89
Bing, L., Béthermin, M., Lagache, G., et al. 2023, A&A, 677, A66
Birkin, J. E., Hutchison, T. A., Welch, B., et al. 2023, ApJ, 958, 64
Blain, A. W., Smail, I., Ivison, R. J., Kneib, J. P., & Frayer, D. T. 2002, PhR, 369, 111
Boquien, M., Burgarella, D., Roehlly, Y., et al. 2019, A&A, 622, A103
Bradley, L., Sipőcz, B., Robitaille, T., et al. 2023, astropy/photutils: v1.8.0, Zenodo, doi:10.5281/zenodo.7946442
Brammer, G. B., van Dokkum, P. G., & Coppi, P. 2008, ApJ, 686, 1503
Burgarella, D., Buat, V., & Iglesias-Páramo, J. 2005, MNRAS, 360, 1413
Bushouse, H., Eisenhamer, J., Dencheva, N., et al. 2023, JWST Calibration Pipeline, v1.12.1, Zenodo, doi:10.5281/zenodo.8380331
Calzetti, D., Armus, L., Bohlin, R. C., et al. 2000, ApJ, 533, 682
Capak, P., Aussel, H., Ajiki, M., et al. 2007, ApJS, 172, 99
Carnall, A. C., McLure, R. J., Dunlop, J. S., & Davé, R. 2018, MNRAS, 480, 4379
Casey, C. M. 2016, ApJ, 824, 36
Casey, C. M. 2020, ApJ, 900, 68
Casey, C. M., Hodge, J., Zavala, J. A., et al. 2018a, ApJ, 862, 78
Casey, C. M., Kartaltepe, J. S., Drakos, N. E., et al. 2023, ApJ, 954, 31
Casey, C. M., Narayanan, D., & Cooray, A. 2014, PhR, 541, 45
Casey, C. M., Zavala, J. A., Aravena, M., et al. 2019, ApJ, 887, 55
Casey, C. M., Zavala, J. A., Manning, S. M., et al. 2021, ApJ, 923, 215
Casey, C. M., Zavala, J. A., Spilker, J., et al. 2018b, ApJ, 862, 77
Chabrier, G. 2003, PASP, 115, 763
Chen, C.-C., Liao, C.-L., Smail, I., et al. 2022, ApJ, 929, 159
Civano, F., Marchesi, S., Comastri, A., et al. 2016, ApJ, 819, 62
Cooper, O. R., Casey, C. M., Zavala, J. A., et al. 2022, ApJ, 930, 32
Cowie, L. L., Barger, A. J., & Bauer, F. E. 2023, ApJ, 952, 28
Enia, A., Talia, M., Pozzi, F., et al. 2022, ApJ, 927, 204
Euclid Collaboration, Moneti, A., McCracken, H. J., et al. 2022, A&A, 658, A126
Fudamoto, Y., Oesch, P. A., Magnelli, B., et al. 2020, MNRAS, 491, 4724
Gentile, F., Talia, M., Behiri, M., et al. 2024a, ApJ, 962, 26
Gentile, F., Talia, M., Daddi, E., et al. 2024b, A&A, 687, A288
Gillman, S., Gullberg, B., Brammer, G., et al. 2023, A&A, 676, A26
Gottumukkala, R., Barrufet, L., Oesch, P. A., et al. 2024, MNRAS, 530, 966
Hasinger, G., Capak, P., Salvato, M., et al. 2018, ApJ, 858, 77
Hayward, C. C., Sparre, M., Chapman, S. C., et al. 2021, MNRAS, 502, 2922
Heintz, E., & Zweibel, E. G. 2022, ApJ, 941, 78
Herard-Demanche, T., Bouwens, R. J., Oesch, P. A., et al. 2025, MNRAS, 537, 788
Heywood, I., Jarvis, M. J., Hale, C. L., et al. 2022, MNRAS, 509, 2150
Hickox, R. C., Wardlow, J. L., Smail, I., et al. 2012, MNRAS, 421, 284
Hodge, J. A., & da Cunha, E. 2020, RSOS, 7, 200556
Hodge, J. A., Swinbank, A. M., Simpson, J. M., et al. 2016, ApJ, 833, 103
Hygate, A. P. S., Hodge, J. A., da Cunha, E., et al. 2023, MNRAS, 524, 1775
Jiménez-Andrade, E. F., Zavala, J. A., Magnelli, B., et al. 2020, ApJ, 890, 171
Jin, S., Daddi, E., Magdis, G. E., et al. 2019, ApJ, 887, 144
Jin, S., Sillassen, N. B., Hodge, J., et al. 2024, A&A, 690, L16
Khostovan, A. A., Kartaltepe, J. S., Salvato, M., et al. 2026, ApJS, 282, 6
Koekemoer, A. M., Aussel, H., Calzetti, D., et al. 2007, ApJS, 172, 196
Kriek, M., Shapley, A. E., Reddy, N. A., et al. 2015, ApJS, 218, 15
Lagos, C. d. P., da Cunha, E., Robotham, A. S. G., et al. 2020, MNRAS, 499, 1948
Leja, J., Carnall, A. C., Johnson, B. D., Conroy, C., & Speagle, J. S. 2019, ApJ, 876, 3
Lewis, A. J. R., Ivison, R. J., Best, P. N., et al. 2018, ApJ, 862, 96
Lilly, S. J., Le Fèvre, O., Renzini, A., et al. 2007, ApJS, 172, 70
Lim, S., Scott, D., Babul, A., et al. 2021, MNRAS, 501, 1803
Liu, F. S., Jia, M., Yesuf, H. M., et al. 2018, ApJ, 860, 60
Long, A. S., Casey, C. M., del P. Lagos, C., et al. 2023, ApJ, 953, 11
Long, A. S., Cooray, A., Ma, J., et al. 2020, ApJ, 898, 133
Madau, P., & Dickinson, M. 2014, ARA&A, 52, 415
Magnelli, B., Karim, A., Staguhn, J., et al. 2019, ApJ, 877, 45
Manning, S. M., Casey, C. M., Zavala, J. A., et al. 2022, ApJ, 925, 23
Manning, S. M., McKinney, J., Whitaker, K. E., et al. 2025, arXiv:2505.09703
Marrone, D. P., Spilker, J. S., Hayward, C. C., et al. 2018, Natur, 553, 51
Marsan, Z. C., Marchesini, D., Brammer, G. B., et al. 2017, ApJ, 842, 21
McCracken, H. J., Milvang-Jensen, B., Dunlop, J., et al. 2012, A&A, 544, A156
McKinney, J., Casey, C. M., Long, A. S., et al. 2025, ApJ, 979, 229
McKinney, J., Manning, S. M., Cooper, O. R., et al. 2023, ApJ, 956, 72
Michałowski, M. J., Dunlop, J. S., Koprowski, M. P., et al. 2017, MNRAS, 469, 492
Moster, B. P., Somerville, R. S., Newman, J. A., & Rix, H.-W. 2011, ApJ, 731, 113
Nanayakkara, T., Glazebrook, K., Kacprzak, G. G., et al. 2016, ApJ, 828, 21
Noll, S., Burgarella, D., Giovannoli, E., et al. 2009, A&A, 507, 1793
Oliver, S. J., Bock, J., Altieri, B., et al. 2012, MNRAS, 424, 1614
Planck Collaboration, Aghanim, N., Akrami, Y., et al. 2020, A&A, 641, A6
Reuter, C., Vieira, J. D., Spilker, J. S., et al. 2020, ApJ, 902, 78
Scoville, N., Aussel, H., Brusa, M., et al. 2007, ApJS, 172, 1
Shen, X., Vogelsberger, M., Nelson, D., et al. 2022, MNRAS, 510, 5560
Simpson, J. M., Smail, I., Swinbank, A. M., et al. 2019, ApJ, 880, 43
Smail, I., Ivison, R. J., & Blain, A. W. 1997, ApJL, 490, L5
Smolčić, V., Novak, M., Bondi, M., et al. 2017, A&A, 602, A1
Staguhn, J. G., Kovács, A., Arendt, R. G., et al. 2014, ApJ, 790, 77
Stott, J. P., Swinbank, A. M., Johnson, H. L., et al. 2016, MNRAS, 457, 1888
Talia, M., Cimatti, A., Giulietti, M., et al. 2021, ApJ, 909, 23
Toft, S., Smolčić, V., Magnelli, B., et al. 2014, ApJ, 782, 68
Trump, J. R., Impey, C. D., McCarthy, P. J., et al. 2007, ApJS, 172, 383
Valentino, F., Brammer, G., Gould, K. M. L., et al. 2023, ApJ, 947, 20
Valentino, F., Tanaka, M., Davidzon, I., et al. 2020, ApJ, 889, 93
van der Vlugt, D., Hodge, J. A., Jin, S., et al. 2023, ApJ, 951, 131
Walter, F., Decarli, R., Carilli, C., et al. 2012, Natur, 486, 233
Wang, T., Schreiber, C., Elbaz, D., et al. 2019, Natur, 572, 211

Weaver, J. R., Cutler, S. E., Pan, R., et al. 2024, ApJS, 270, 7
Weaver, J. R., Kauffmann, O. B., Ilbert, O., et al. 2022, ApJS, 258, 11
Williams, C. C., Labbe, I., Spilker, J., et al. 2019, ApJ, 884, 154
Wisnioski, E., Förster Schreiber, N. M., Fossati, M., et al. 2019, ApJ, 886, 124
Xiao, M. Y., Elbaz, D., Gómez-Guijarro, C., et al. 2023, A&A, 672, A18
Xiao, M. Y., Oesch, P., Elbaz, D., et al. 2024, Natur, 635, 311
Yun, M. S., Aretxaga, I., Gurwell, M. A., et al. 2015, MNRAS, 454, 3485
Zavala, J. A., Casey, C. M., da Cunha, E., et al. 2018a, ApJ, 869, 71
Zavala, J. A., Casey, C. M., Manning, S. M., et al. 2021, ApJ, 909, 165
Zavala, J. A., Montaña, A., Hughes, D. H., et al. 2018b, NatAs, 2, 56
Zimmerman, D. T., Narayanan, D., Whitaker, K. E., & Davè, R. 2024, ApJ, 973, 146